Electronic Supplementary Information

Tetracationic phosphonium-bridged ladder stilbenes: Redox states and electronic properties of highly charged P-heteropolycyclic materials

Sebastian Senn[a], Nele Konrad[b], Jens Müller[b], Joachim Ballmann[†a] and Lutz H. Gade*[a]

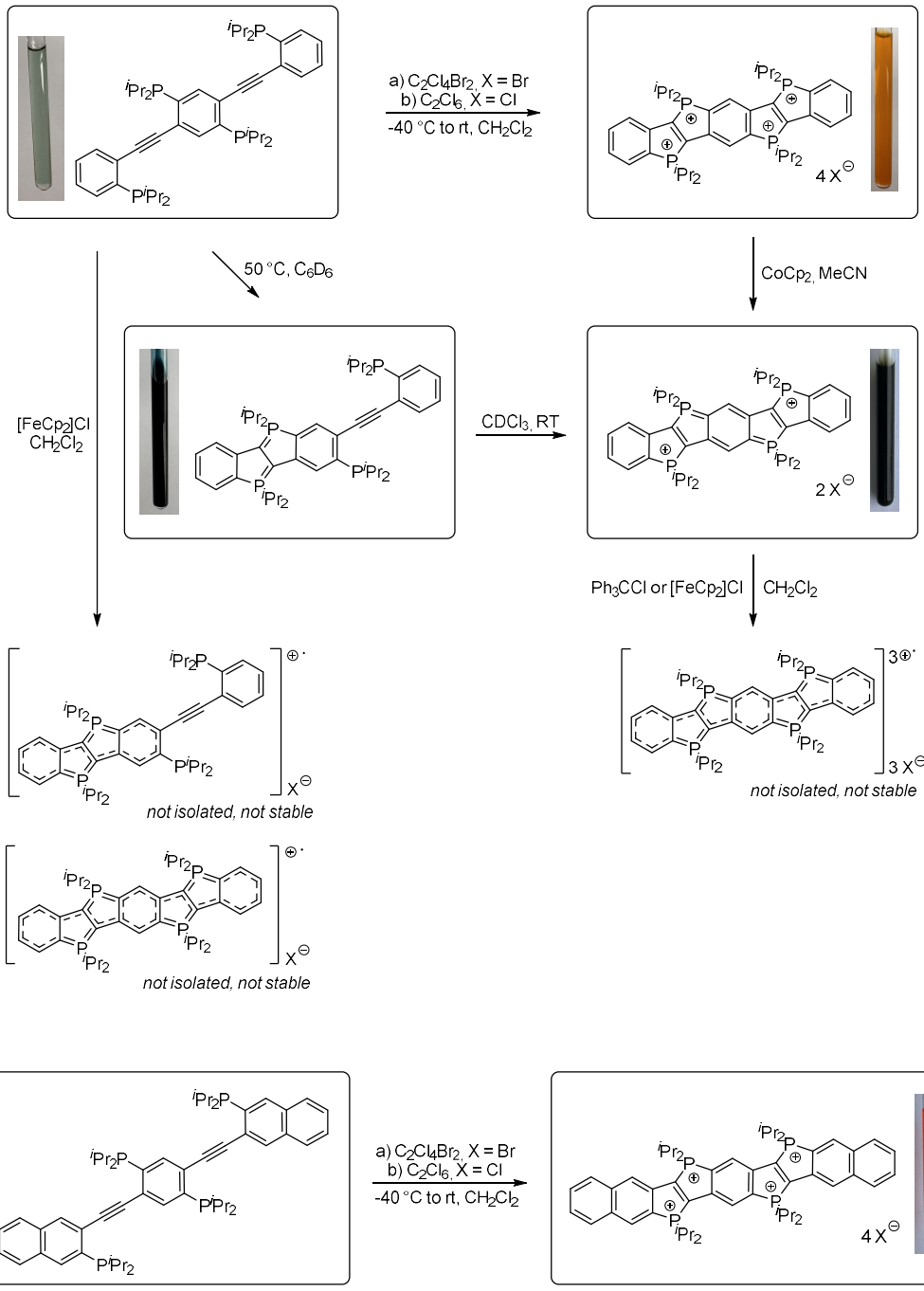
a) C2Cl4Br2, X = Br
b) C2Cl6, X = Cl
-40 °C to rt, CH2Cl2
4 X⊖
50 °C, C6D6
CoCp2, MeCN
[FeCp2]Cl
CH2Cl2
CDCl3, RT
2 X⊖
Ph3CCl or [FeCp2]Cl
CH2Cl2
3 X⊖
not isolated, not stable
or
not isolated, not stable
not isolated, not stable
a) C2Cl4Br2, X = Br
b) C2Cl6, X = Cl
-40 °C to rt, CH2Cl2
4 X⊖

1) Table of Contents

2) Experimental Procedures

2.1) General Remarks

Synthetic experiments were carried out under dry and oxygen-free argon (argon 5.0, dried over a column of phosphorus pentoxide). For air-sensitive compounds, standard Schlenk techniques were applied or a glovebox (MBraun) was used. Schlenk glassware was flame-dried prior to use. Solvents were dried according to standard procedures. All solvents and chemicals were purchased from commercial suppliers and used as received without further purification. Deuterated solvents were dried over calcium hydride (CD_2Cl_2) or sodium (benzene-d_6, THF-d_8, toluene-d_8) and distilled. ^1H, ^{31}P, and ^{13}C NMR spectra were recorded on a Bruker Avance II 400 MHz or a Bruker Avance 600 III spectrometer and referenced to the residual (undeuterated) solvent signal (for ^1H and ^{13}C NMR). ^{31}P NMR spectra were referenced to external $P(OMe)_3$ (141.0 ppm; 85% H_3PO_4 at 0.0 ppm). Heteronuclear spectra were recorded with ^1H broadband or composite pulse decoupling unless otherwise specified. Chemical shifts (δ) are reported in parts per million (ppm), and coupling constants (J) in Hertz (Hz). Common abbreviations were used to describe multiplicities (e.g., s = singlet, bs = broad singlet, d = doublet, dd = doublet of doublets, m = multiplet). NMR spectra were processed using MestReNova. Mass spectra were recorded at the Department of Organic Chemistry, Heidelberg University, under the direction of Dr. J. Gross. Spectra were measured using a Bruker Autoflex Speed MALDI-TOF for MALDI HRMS, a Bruker timsTOF fleX for ESI HRMS, and a JEOL JMS-700 magnetic-sector instrument employing the liquid injection field desorption ionization (LIFDI) technique. Elemental analyses were performed at the Department of Inorganic Chemistry, Heidelberg University, on an Elementar vario MICRO Cube. Absorption spectra were recorded on a Cary 5000 UV/Vis spectrometer with baseline and solvent correction. Fluorescence spectra were obtained using a Varian Cary Eclipse fluorescence spectrophotometer. IR spectra were recorded on an Agilent Cary 630 FTIR. Cyclic voltammograms were recorded with a PalmSens EmStat3 Blue instrument under inert atmosphere inside the glovebox. Graphite (working), platinum wire (counter), and silver wire (reference) electrodes were used. All spectra were referenced against ferrocene (internal standard). Measurements were carried out in a 0.1 M tetrabutylammonium trifluoromethanesulfonate solution in anhydrous acetonitrile. X-band EPR spectra were recorded on a Magnettech MiniScope MS400 spectrometer (room temperature) under inert atmosphere (Ar) and simulated using EasySpin v6.0.9 and MATLAB R2025a.[1-3] Zero-field splitting parameters were obtained by fitting to the experimental data. Analytical data were plotted using OriginPro 2021 (64-bit).

2.2) Synthesis of Compounds

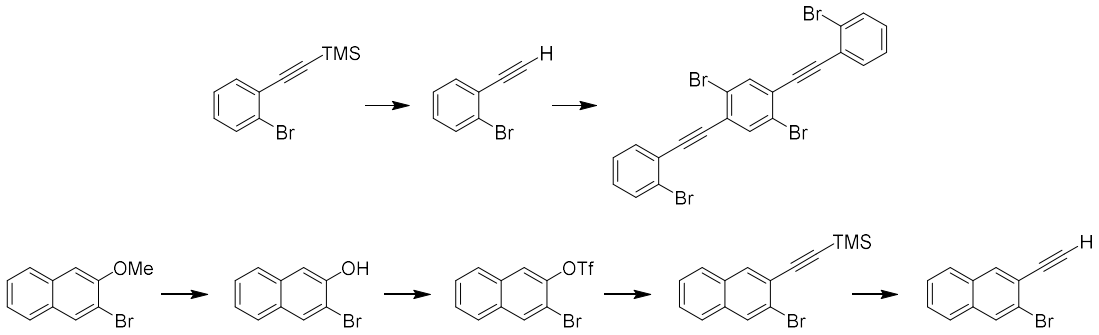

The literature known compounds ((2-Bromophenyl)ethynyl)trimethylsilane[4], 1-Bromo-2-ethynylbenzene[5], 2,2'-((2,5-Dibromo-1,4-phenylene)bis(ethyne-2,1-diyl))bis(bromobenzene)[6], 2-Bromo-3-methoxynaphthalene[7], 3-Bromonaphthalen-2-ol[7], 3-Bromonaphthalen-2-yl trifluoromethanesulfonate[8], ((3-Bromonaphthalen-2-yl)ethynyl)trimethylsilane[9] were synthesized according to published literature procedures.

2-Bromo-3-ethynylnaphthalene was synthesized analogously to the published procedure of 1-Bromo-2-ethynylbenzene[5]. In a round bottom flask ((3-bromonaphthalen-2-yl)ethynyl)trimethylsilane (1.41 g, 4.66 mmol), and Potassium hydroxide (1.05 g, 18.7 mmol, 4.00 eq) were dissolved in methanol (100 mL). The mixture was stirred at rt for 16 h. Addition of a 2 M HCl-solution (aq., 30 mL) completed the reaction. The mixture was extracted (3 × 100 mL petroleum ether), washed (brine), dried ($MgSO_4$) and filtered. The solvent was removed under reduced pressure. Without further purification 2-Bromo-3-ethynylnaphthalene was afforded as an off-white solid (1.03 g, 4.46 mmol, 96%). **^{1}H NMR** (600 MHz, $CDCl_3$): δ (in ppm) = 8.09 (s, 1H), 8.07 (s, 1H), 7.78–7.73 (m, 2H), 7.54–7.49 (m, 2H), 3.40 (s, 1H). *These data are in accordance with the literature*.[10]

3,3'-((2,5-Dibromo-1,4-phenylene)bis(ethyne-2,1-diyl))bis(2-bromonaphthalene). 1,4-Dibromo-2,5-diiodobenzene (820 mg, 1.68 mmol), 2-Bromo-3-ethynylnaphthalene (797 mg, 3.45 mmol, 2.05 eq) and $PdCl_2(PPh_3)_2$ (5 mol%, 59 mg, 84.1 µmol) were dissolved in a mixture of N,N-Dimethylformamide (40 mL) and $^i Pr_2NH$ (12 mL). CuI (5 mol%, 16 mg, 84.1 µmol) was added, and the mixture was stirred at rt for 72 h. The crude product was filtered off and washed with dichloromethane (25 mL). Recrystallization from hot 1,4-dioxane after hot filtration afforded compound **4** as an off-white solid (826 mg, 1.19 mmol, 71%). **MP**: 214 °C (decomp.). **ATR-IR** (selected peaks): ν [cm^{-1}] = 3053, 2216, 1582, 1493, 1426, 1360, 1269, 1193, 1128, 1059, 991, 947, 893, 870, 798, 738.**^{1}H NMR** (400 MHz, $CDCl_3$): δ (in ppm) = 8.16 (s, 2H), 8.14 (s, 2H), 7.90 (s, 2H), 7.84–7.81 (m, 2H), 7.78–7.75 (m, 2H), 7.55–7.52 (m, 4H). **MALDI HR-MS** (pos): *m/z* calcd for $C_{30}H_{14}Br_4^+$ $[M]^+$ 689.7824, found 689.7825. *Due to very low solubility, it was not possible to measure a reasonably resolved $^{13}C\{^1H\}$ NMR spectrum.*

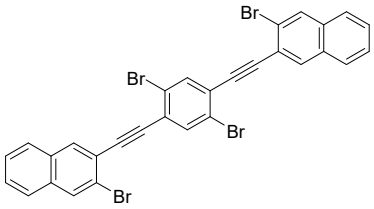

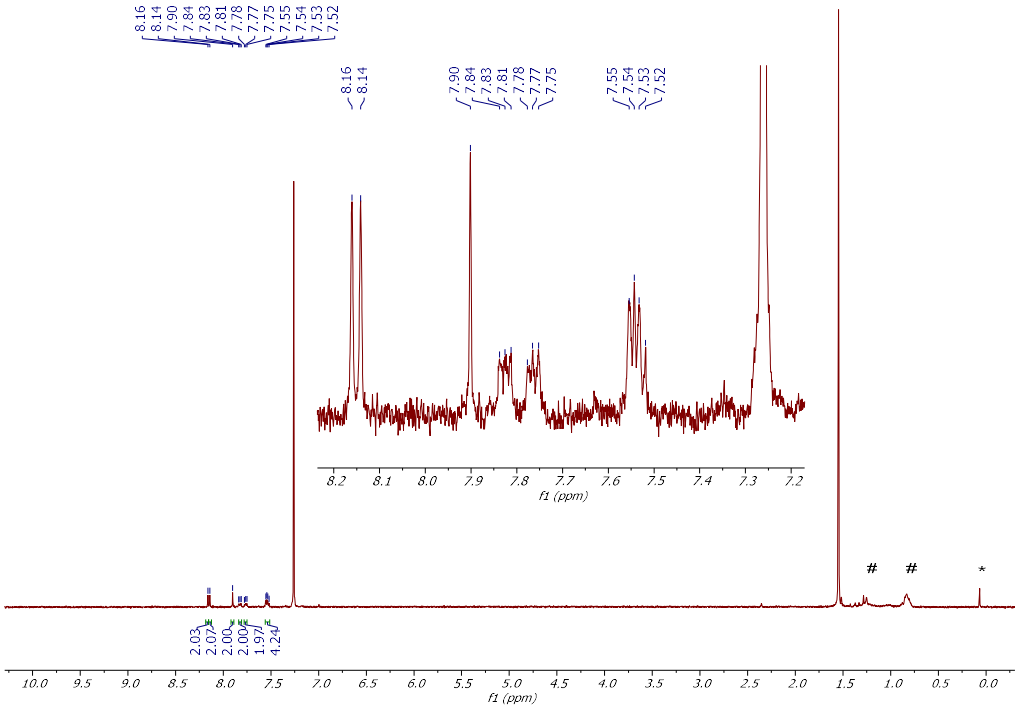

Figure 1: ^{1}H NMR spectrum (400 MHz, $CDCl_3$, 298K) of **4** (traces of impurities of silicon grease (*) and paraffin oil (#) are marked).

(2,5-bis((2-(diisopropylphosphaneyl)phenyl)ethynyl)-1,4-phenylene)bis(diisopropylphosphane). In a flame-dried and argon-filled ampulla compound **3** (800 mg, 1.35 mmol) was dissolved in dry thf (40 mL). A 1.7 M solution of *t*-BuLi in hexanes (6.34 ml, 10.8 mmol, 8.00 eq.) was added dropwise at –78 °C. The mixture was stirred for 2.0 h at this temperature and $^{i}Pr_2PCl$ (1.23 g, 1.29 mL, 8.08 mmol, 6.00 eq) was added dropwise. The reaction mixture was stirred in cryostat at –8 °C for 16 h. Conversion was confirmed via ^{31}P NMR spectroscopy, and the solvent was removed under reduced pressure. Inside the glovebox the crude mixture was suspended in toluene and filtered over Celite. Recrystallization from dry toluene (–40 °C) afforded compound **5** as off-white solid (731 mg, 73%). **MP**: 121 °C (decomp.). **ATR-IR** (selected peaks): ν [cm^{-1}] = 2948, 2922, 2896, 2863, 1476, 1457, 1383, 1360, 1241, 1152, 1032, 1018, 876, 753, 731, 656. **^{1}H NMR** (600 MHz, thf-d_8): δ (in ppm) = 7.89–7.88 (m, 2H), 7.65–7.63 (m, 2 H), 7.55–7.52 (m, 2H), 7.36–7.32 (m, 4H), 2.37–2.31 (m, 8H), 1.21–1.16 (m, 24H), 1.04–0.95 (m, 24H). **^{31}P {^{1}H} NMR** (243 MHz, thf-d_8): δ (in ppm) = 4.9 (s, 2P), 3.0 (s, 2P). **^{13}C {^{1}H} NMR** (151 MHz, thf-d_8): δ (in ppm) = 140.1 (d, $J_{C\text{-}P}$ = 23.1 Hz, C_q, 2C), 139.5 (d, $J_{C\text{-}P}$ = 25.5 Hz, C_q, 2C), 138.4 (CH, 2C), 134.5 (d, $J_{C\text{-}P}$ = 6.1 Hz, CH, 2C), 133.7 (d, $J_{C\text{-}P}$ = 4.1 Hz, CH, 2C), 131.5 (d, $J_{C\text{-}P}$ = 25.6 Hz, C_q, 2C), 130.6 (d, $J_{C\text{-}P}$ = 27.3 Hz, C_q, 2C), 129.4 (CH, 2C), 128.6 (d, $J_{C\text{-}P}$ = 2.6 Hz, CH, 2C), 97.5 (dd, $J_{C\text{-}P}$ = 6.9, 2.3 Hz, C_q, 2C), 95.8 (dd, $J_{C\text{-}P}$ = 6.1, 2.5 Hz, C_q, 2C), 24.7–24.5 (m, CH, 8C), 21.0–20.6 (m, CH_3, 8C), 20.3–20.2 (m, CH_3, 8C). **Anal. Calcd. for** $C_{46}H_{66}P_4$ (742.9 g/mol): C 74.37, H 8.95. Found: C 74.42, H 9.20. **LIFDI** (pos): *m/z* calcd for $C_{46}H_{66}P_4^+$ $[M]^+$ 742.4110, found 742.4553.

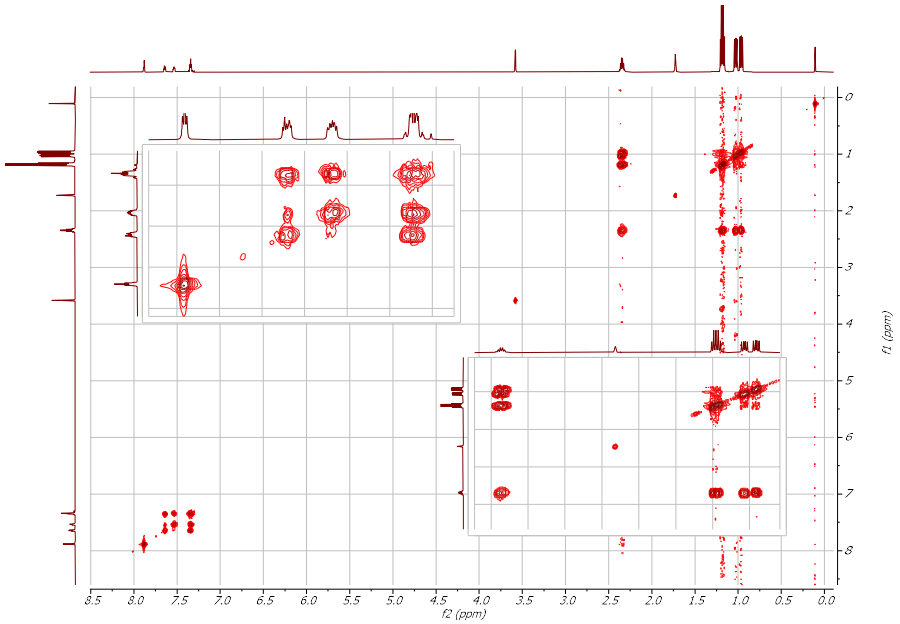

Figure 2: $^{1}H^{1}H$-Cosy NMR spectrum (600 MHz, thf-d_8, 298K) of **5**.

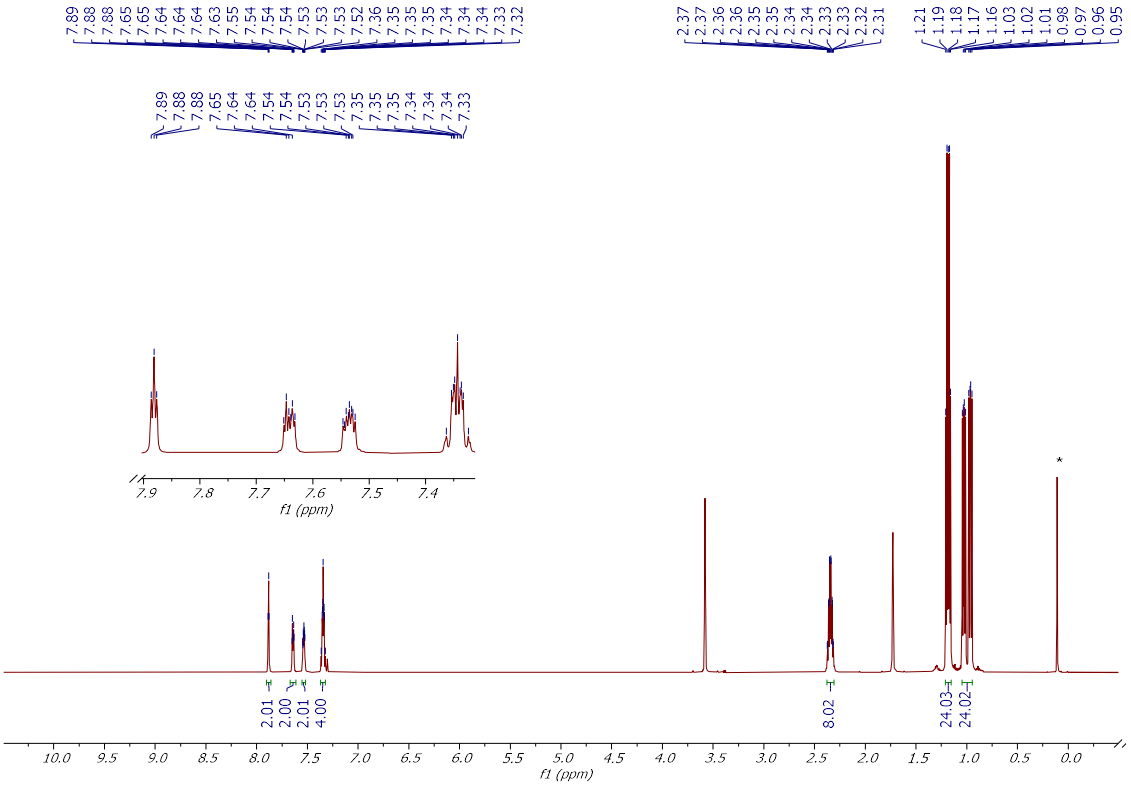

Figure 3: ^{1}H NMR spectrum (600 MHz, thf-d_8, 298K) of **5** (traces of impurities of silicon grease (*) are marked).

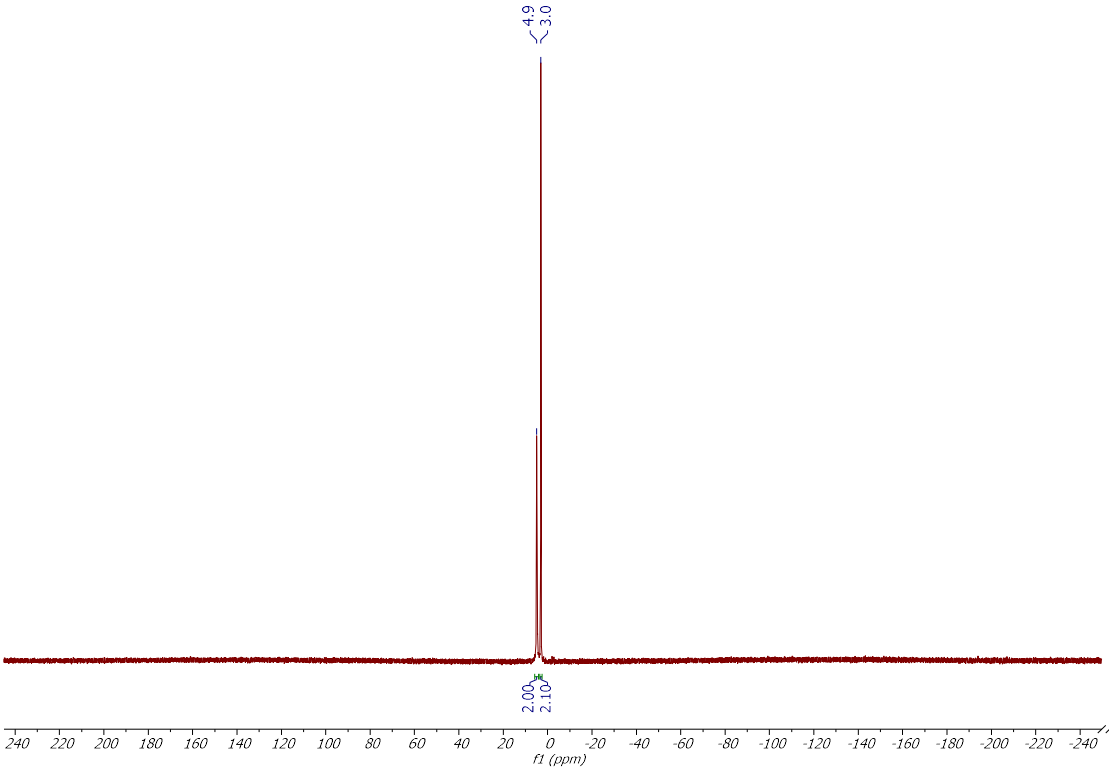

Figure 4: $^{31}P\{^{1}H\}$ NMR spectrum (243 MHz, thf-d_8, 298K) of **5**.

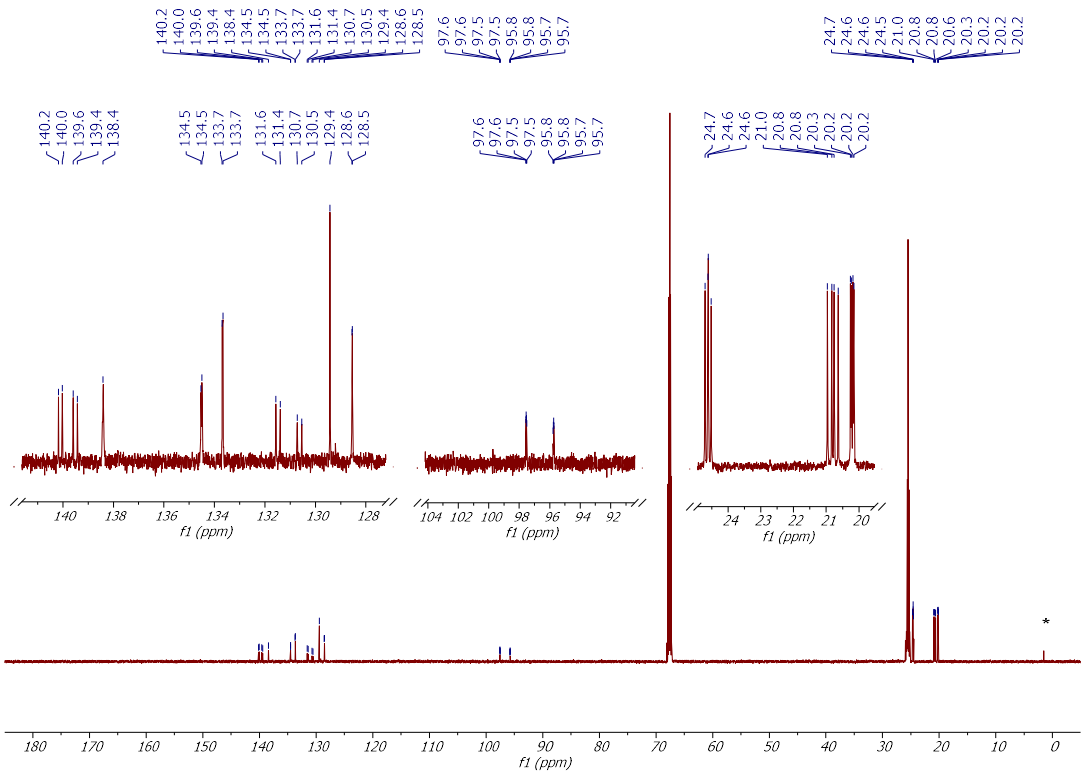

Figure 5: $^{13}C\{^{1}H\}$ NMR spectrum (151 MHz, thf-d_8, 298K) of **5** (traces of impurities of silicon grease (*) are marked).

3-(diisopropylphosphaneyl)-2-((2-(diisopropylphosphaneyl)phenyl)ethynyl)-5,5,10,10-tetraisopropyl-5l5,10l5-phosphindolo[3,2-b]phosphindole. 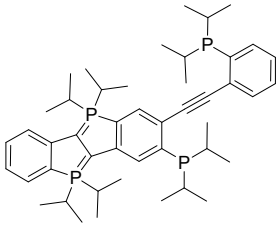

Inside the glovebox compound **5** (10.0 mg, 13.5 µmol) was dissolved in dry thf-d_8 (0.5 mL). The mixture was heated up to 50 °C for 5 h 30 min. Conversion was confirmed via ^{31}P NMR and ^{1}H NMR spectroscopy. The crude mixture was filtered through a syringe filter, and the solvent was removed under reduced pressure. Compound **10** was afforded as dark blue solid (9.40 mg, 94%). **MP**: 138 °C (decomp.). **ATR-IR** (selected peaks): ν [cm^{-1}] = 2952, 2922, 2864, 2167, 1577, 1545, 1452, 1415, 1333, 1232, 1126, 1114, 1051, 1012, 904, 876, 811, 755, 729, 656. **^{1}H NMR** (600 MHz, thf-d_8): δ (in ppm) = 7.45–7.43 (m, 1H), 7.41–7.38 (m, 1H), 7.33–7.31 (m, 1H), 7.21–7.18 (m, 1H), 7.09 (td, J_{H-H} = 7.5, 1.4 Hz, 1H), 7.00–6.98 (m, 1H), 6.66 (dd, J_{H-P} = 7.6, 3.8 Hz, 1H), 6.61–6.60 (m, 2H), 6.01–5.98 (m, 1H), 2.77–2.70 (m, 4H), 2.43–2.34 (m, 2H), 1.21–1.12 (m, 36H), 1.03–1.00 (m, 6H), 0.96–0.93 (m, 6H).**^{31}P {^{1}H} NMR** (243 MHz, thf-d_8): δ (in ppm) = 26.4 (d, J_{P-P} = 31.6 Hz, 1P), 25.3 (dd, J_{P-P} = 31.6, 1.4 Hz, 1P), 14.2 (s, 1P), 5.4 (s, 1P). **^{13}C {^{1}H} NMR** (151 MHz, thf-d_8): δ (in ppm) = 150.6–150.4 (m, C_q, 1C), 144.6–144.5 (m, C_q, 1C), 138.4–138.3 (m, CH, 1C), 137.5 (d, J_{C-P} = 21.0 Hz, C_q, 1C), 135.1 (d, J_{C-P} = 19.6 Hz, C_q, 1C), 134.7 (d, J_{C-P} = 11.6 Hz, CH, 1C), 133.4 (d, J_{C-P} = 21.9 Hz, C_q, 1C), 132.3–132.2 (m, CH, 2C), 130.1 (CH, 1C), 129.0 (CH, 1C), 125.7 (d, J_{C-P} = 4.3 Hz, CH, 1C), 124.7 (CH, 1C), 118.0 (d, J_{C-P} = 7.0 Hz, CH, 1C), 113.0 (d, J_{C-P} = 11.7 Hz, CH, 1C), 109.8–109.6 (m, C_q, 1C), 107.1–105.9 (m, C_q, 2C), 101.1–101.1 (m, C_q, 1C), 92.3–92.2 (m, C_q, 1C), 72.3 (dd, J_{C-P} = 111.6, 22.0 Hz, C_q, 1C), 65.0 (dd, J_{C-P} = 116.6, 22.7 Hz, C_q, 1C), 27.4–26.5 (m, CH, 4C), 24.5–24.4 (m, CH, 4C), 21.4–21.0 (m, CH_3, 4C), 20.7–20.6 (m, CH_3, 4C), 17.5–17.2 (m, CH_3, 4C), 17.2–17.1 (m, CH_3, 4C). **Anal. Calcd. for** $C_{46}H_{66}P_4$ (742.9 g/mol): C 74.37, H 8.95. Found: C 74.00, H 8.95. **LIFDI** (pos): *m/z* calcd for $C_{46}H_{66}P_4^+$ $[M]^+$ 742.4110, found 742.4553; *m/z* calcd for $C_{46}H_{66}P_4O_2^+$ $[M+O_2]^+$ 774.4013, found 774.4497.

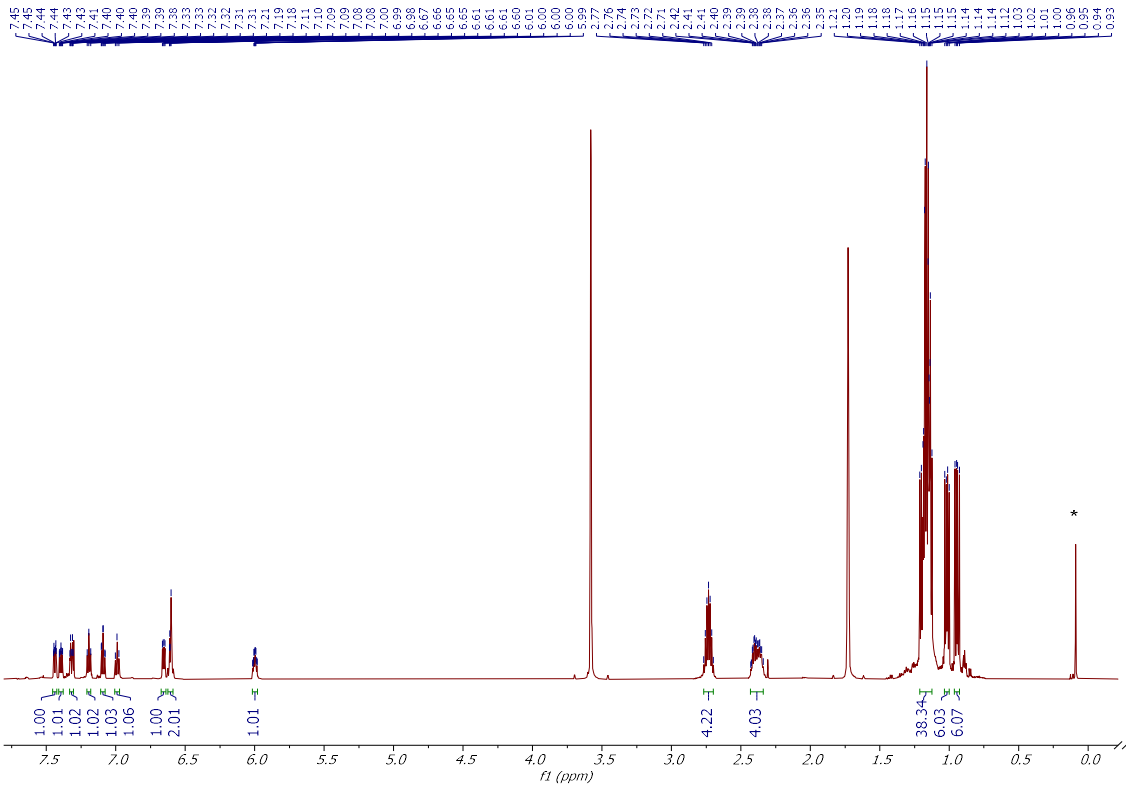

Figure 6: ^{1}H NMR spectrum (600 MHz, thf-d_8, 298K) of **10**.

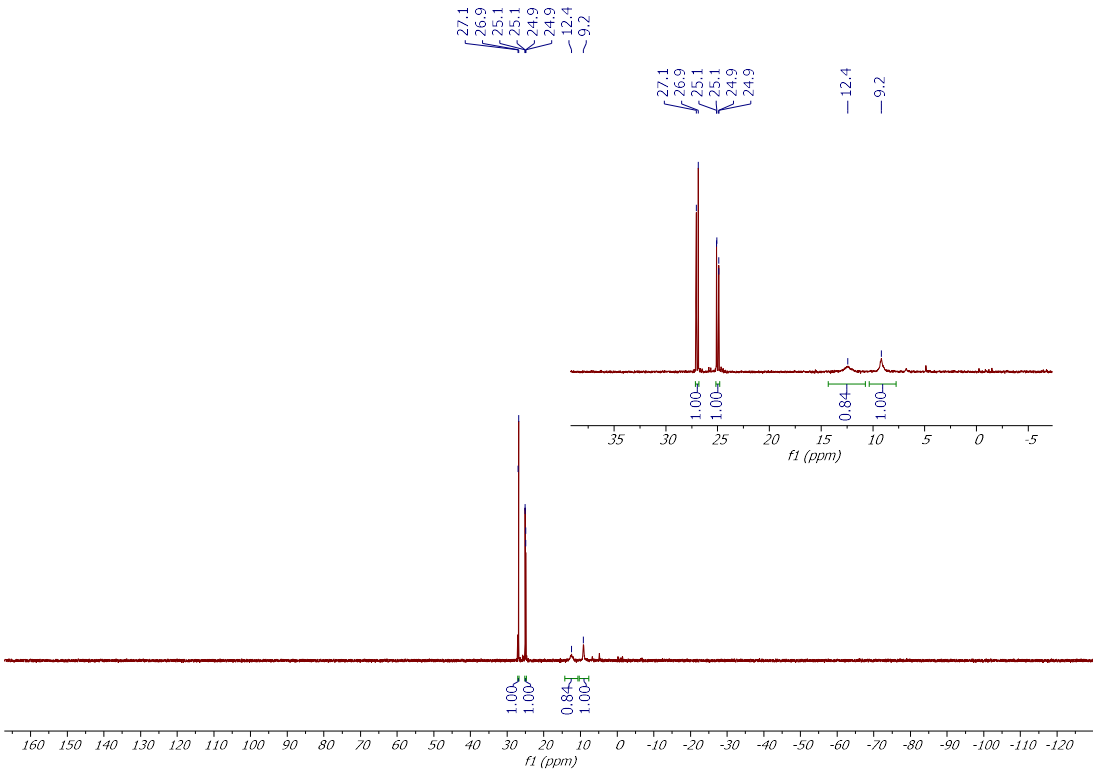

Figure 7: ^{31}P{^{1}H} NMR spectrum (162 MHz, thf-d_8, 298K) of **10**.

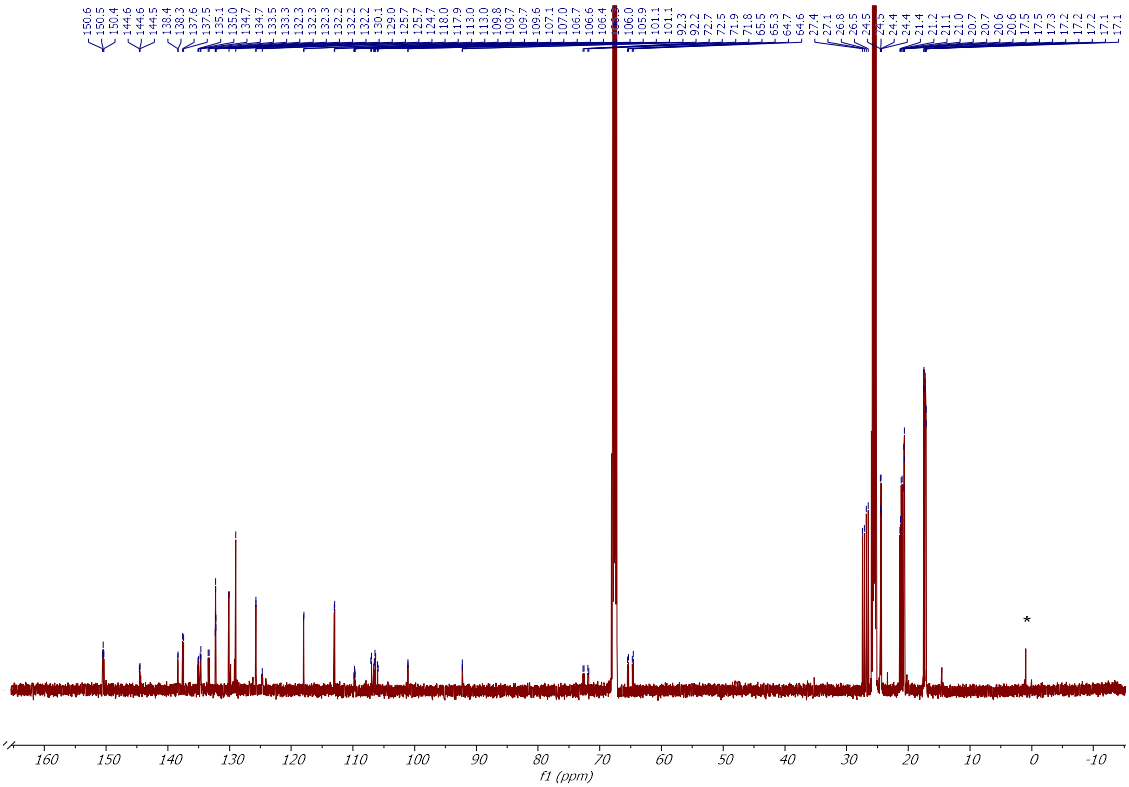

Figure 8: **$^{13}C\{^1H\}$ NMR** spectrum (151 MHz, thf-d_8, 298K) of **10** (traces of impurities of silicon grease (*) are marked).

[PhPhPh]X_2 ***Method A: Oxidation of 10 (X = Cl).*** Inside the glovebox compound **10** (7 mg, 9.42 µmol) was dissolved in dry $CDCl_3$ (0.5 mL) in a *J*-Young NMR tube and stirred at rt on an orbital-stirrer for 10 min. The solvent was removed under reduced pressure and the crude product was washed with thf. Compound [**9**]**Cl_2** was afforded as dark grey solid (3.20 mg, 36%). ***Method B: Reduction of 7 (X = Br).*** Inside the glovebox compound **7** (100 mg, 94.1 µmol) was dissolved in dry MeCN (10 mL). Cp_2Co (35.6 mg, 188 µmol, 2.00 eq.) was added and the mixture was stirred at rt for 16 h. Conversion was confirmed via ^{31}P NMR spectroscopy. The solvent was removed under reduced pressure, and the crude product was washed with thf. Compound [**9**]**Br_2** was afforded as dark grey solid (39.4 mg, 46%). **MP**: 228 °C (decomp.). **ATR-IR** (selected peaks): ν [cm^{-1}] = 3088, 2961, 2861, 1579, 1497, 1437, 1415, 1347, 1331, 1282, 1239, 1204, 1161, 1128, 1051, 1027, 982, 936, 870, 786, 757, 680. **^1H NMR** (600 MHz, CD_2Cl_2): *δ* (in ppm) = 8.17 (d, J_{H-P} = 10.8 Hz, 2H), 7.39–7.37 (m, 2H), 7.31–7.28 (m, 2H), 6.93 (d, J_{H-P} = 8.1 Hz, 2H), 6.82–6.80 (m, 2H), 4.01–3.98 (m, 4H), 3.64–3.61 (m, 4H), 1.41–1.19 (m, 48H). **$^{31}P\{^1H\}$ NMR** (243 MHz, CD_2Cl_2): *δ* (in ppm) = 43.3–43.2 (m, 2P), 41.5–41.4 (m, 2P). **$^{13}C\{^1H\}$ NMR** (151 MHz, CD_2Cl_2): *δ* (in ppm) = 148.9–148.7 (m, C_q, 2C), 134.4 (CH, 2C), 132.7–132.6 (m, CH, 2C), 131.2 (t, J_{C-P} = 9.1 Hz, CH, 2C), 129.7–129.4 (m, C_q, 2C), 120.6–120.5 (m, CH, 2C), 119.8–119.7 (m, CH, 2C), 117.8–117.2 (m, C_q, 2C), 116.1–115.4 (m, C_q, 2C), 113.6–113.0 (m, C_q, 2C), 89.1–88.3 (m, C_q, 2C), 26.7–26.3 (m, CH, 4C), 25.1–24.7 (m, CH, 4C), 17.7

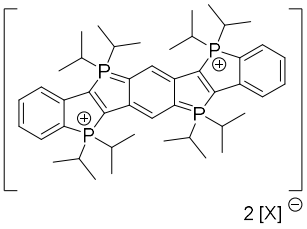

(CH_3, 2C), 17.2 (CH_3, 2C), 17.0 (CH_3, 2C), 16.8 (CH_3, 2C). **MALDI HR-MS** (pos): *m/z* calcd for $C_{46}H_{66}P_4Cl^+$ $[M+Cl]^+$ 777.3798, found 777.3803; calcd for $C_{46}H_{66}P_4Br^+$ $[M+Br]^+$ 821.3293, found 821.3291. *In addition to the expected signal, the mass spectra show features attributable to other oxidation states, likely arising from partial decomposition during the measurement.*

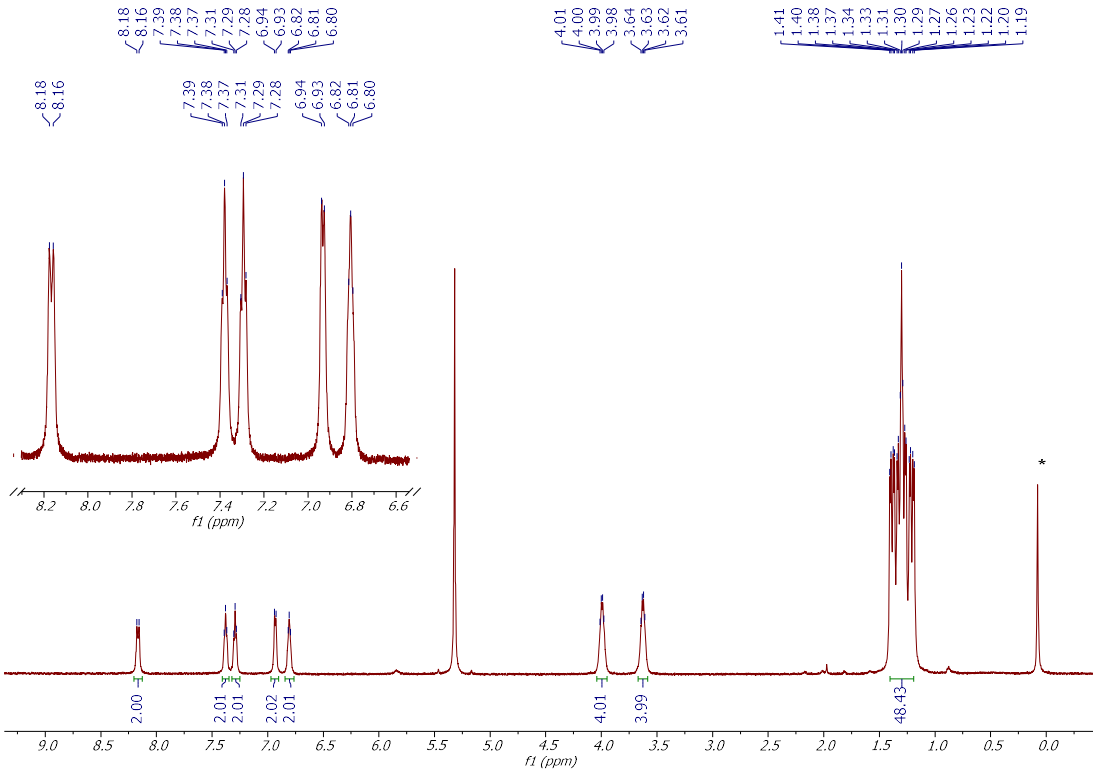

Figure 9: ^{1}H NMR spectrum (600 MHz, CD_2Cl_2, 298K) of **9** (traces of impurities of silicon grease (*) are marked).

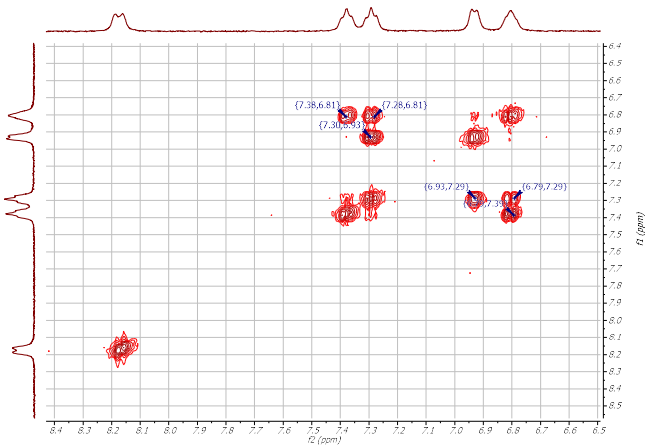

Figure 10: ^{1}H^{1}H-Cosy NMR spectrum (600 MHz, CD_2Cl_2, 298K) of **9**.

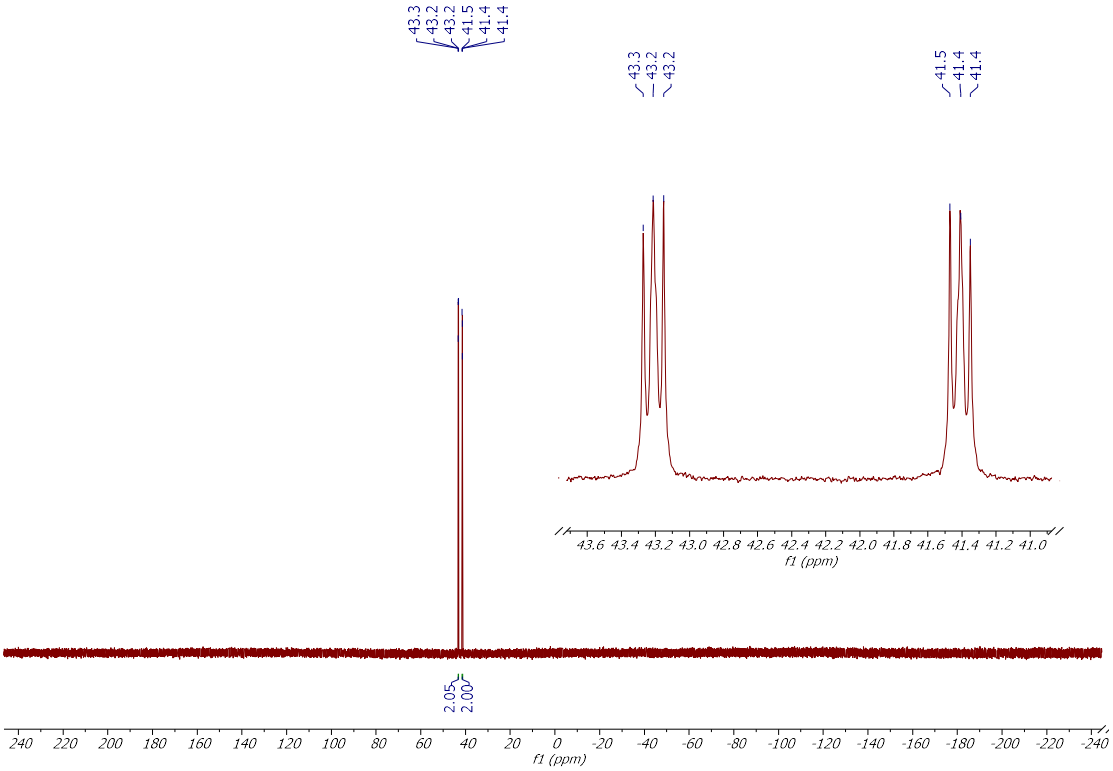

Figure 11a: $^{31}P\{^{1}H\}$ NMR spectrum (243 MHz, CD_2Cl_2, 298K) of **9**.

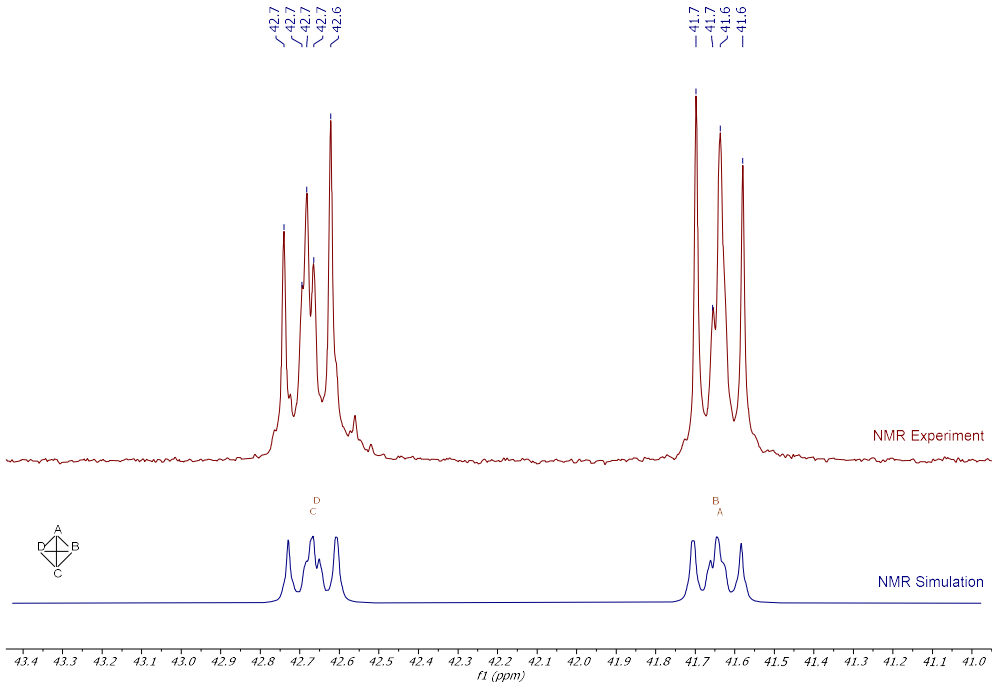

Figure 11b: Experimental **$^{31}P\{^{1}H\}$ NMR** spectrum (243 MHz, **$CDCl_3$**, 298K) of **9** and the corresponding simulation (MestReNova NMR prediction tool; fitting parameters: δ (in ppm) = 41.7054 (A), 41.7164 (B), 42.7156 (C), 42.7057 (D). J_s (in Hz) = 2.53680 (B–A, D–C), 17.67740 (C–A, D–B), 11.34110 (D–A, D–B), simulated assuming **virtual coupling between all four phosphorus nuclei**). Reducing the spectral window to 42.5±15 ppm, increasing the acquisition time by a factor of 20, and using $CDCl_3$ as the solvent afforded a notably higher resolution compared to Figure 11a.

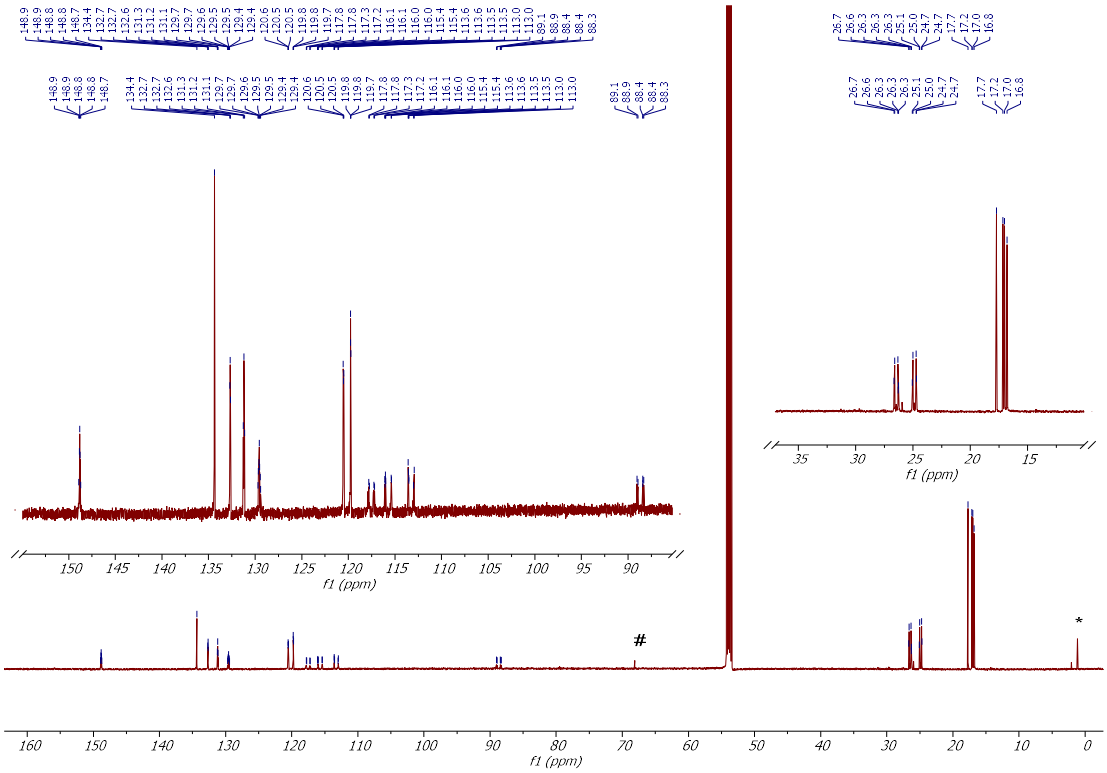

Figure 12: $^{13}C\{^{1}H\}$ NMR spectrum (151 MHz, CH_2Cl_2, 298K) of **9** (traces of impurities of silicon grease (*) and thf (#) are marked).

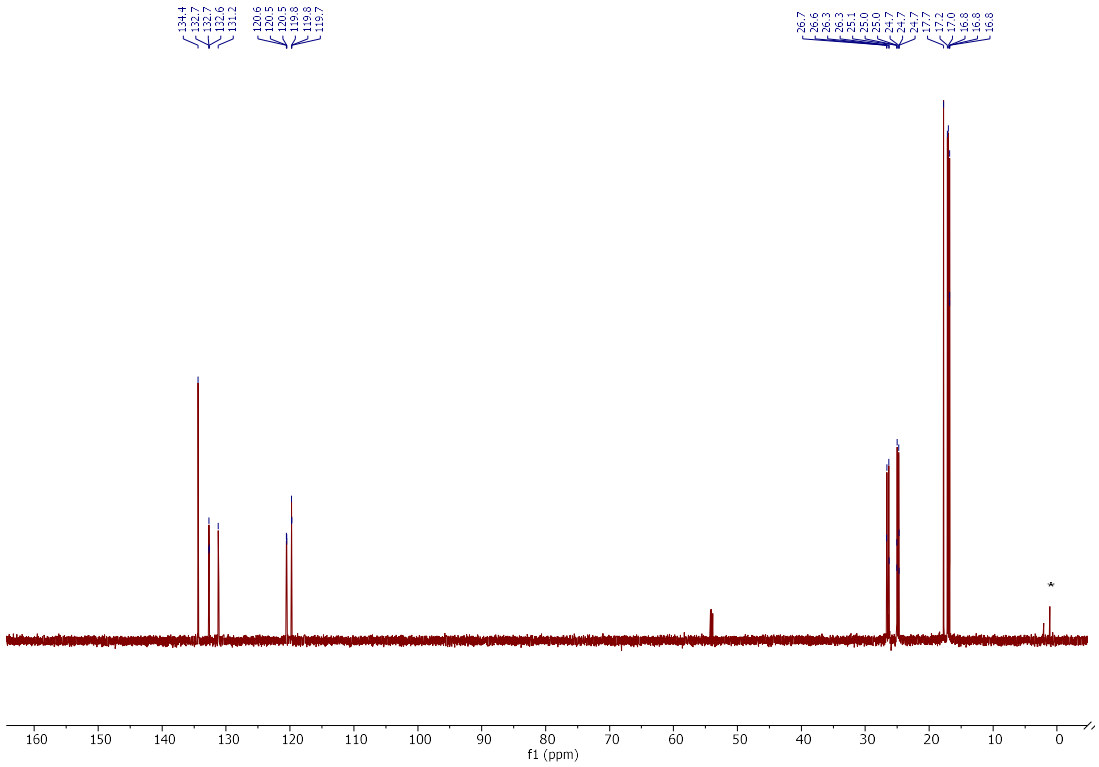

Figure 13: ^{13}C dept-135 NMR spectrum (151 MHz, CH_2Cl_2, 298K) of **9** (traces of impurities of silicon grease (*) are marked).

[PhPhPh]Br$_4$. Inside the glovebox compound **5** (100 mg, 135 µmol) was dissolved in dry CH_2Cl_2 (10 mL) at –40 °C. $C_2Cl_4Br_2$ (43.8 mg, 135 µmol, 1.00 eq.) was added and the mixture was warmed to rt over 30 min. Further $C_2Cl_4Br_2$ (43.8 mg, 135 µmol, 1.00 eq.) was added and the mixture was stirred at rt for 16 h. Conversion was confirmed via ^{31}P NMR spectroscopy. Pentane (10 mL) was added, and the mixture was filtered. Recrystallization from MeOH/Et_2O afforded compound **7** as deep red solid (88.0 mg, 62%).

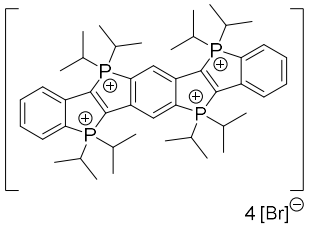

MP: 198 °C (decomp.). **ATR-IR** (selected peaks): ν [cm^{-1}] = 2971, 2837, 1457, 1394, 1375, 1271, 1223, 1163, 1137, 1073, 1051, 924, 880, 768, 719, 697. **^{1}H NMR** (600 MHz, CD_3OD): *δ* (in ppm) = 9.41 (bs, 2H), 8.42 (bs, 2H), 8.19 (bs, 4H), 8.04 (bs, 2H), 4.62 (bs, 4H), 4.54 (bs, 4H), 1.62–1.53 (m, 36H), 1.47–1.42 (m, 12H). **^{31}P {^{1}H} NMR** (162 MHz, CD_3OD): *δ* (in ppm) = 63.0 (d, J_{P-P} = 23.0 Hz, 2P), 60.7 (d, J_{P-P} = 22.7 Hz, 2P). **^{13}C {^{1}H} NMR** (151 MHz, CD_3OD): *δ* (in ppm) = 152.0 (d, J_{C-P} = 56.7 Hz, C_q, 2C), 146.2 (d, J_{C-P} = 71.8 Hz, C_q, 2C), 143.4 (bs, C_q, 2C), 139.6 (bs, C_q, 2C), 138.8 (CH, 2C), 135.9 (bs, CH, 2C), 135.2 (bs, CH, 2C), 133.3 (d, J_{C-P} = 75.9 Hz, C_q, 2C), 132.9 (bs, CH, 2C), 129.8 (CH, 2C), 122.1 (d, J_{C-P} = 84.8 Hz, C_q, 2C), 25.0–24.2 (m, CH, 8C), 17.1–16.1 (m, CH_3, 48C). **MALDI HR-MS** (pos): *m/z* calcd for $C_{46}H_{66}P_4Br_3^+$ [M+3Br]$^+$ 979.1660, found 979.1658.

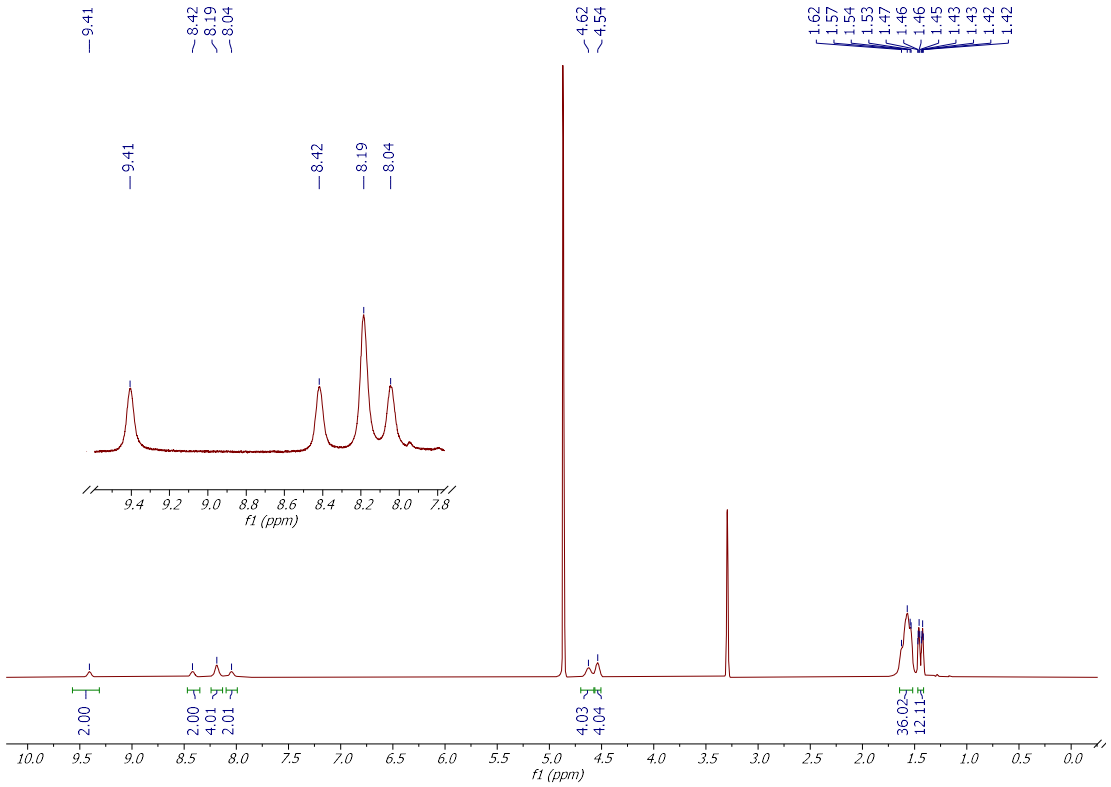

Figure 14: ^{1}H NMR spectrum (600 MHz, CD_3OD, 298K) of **7**.

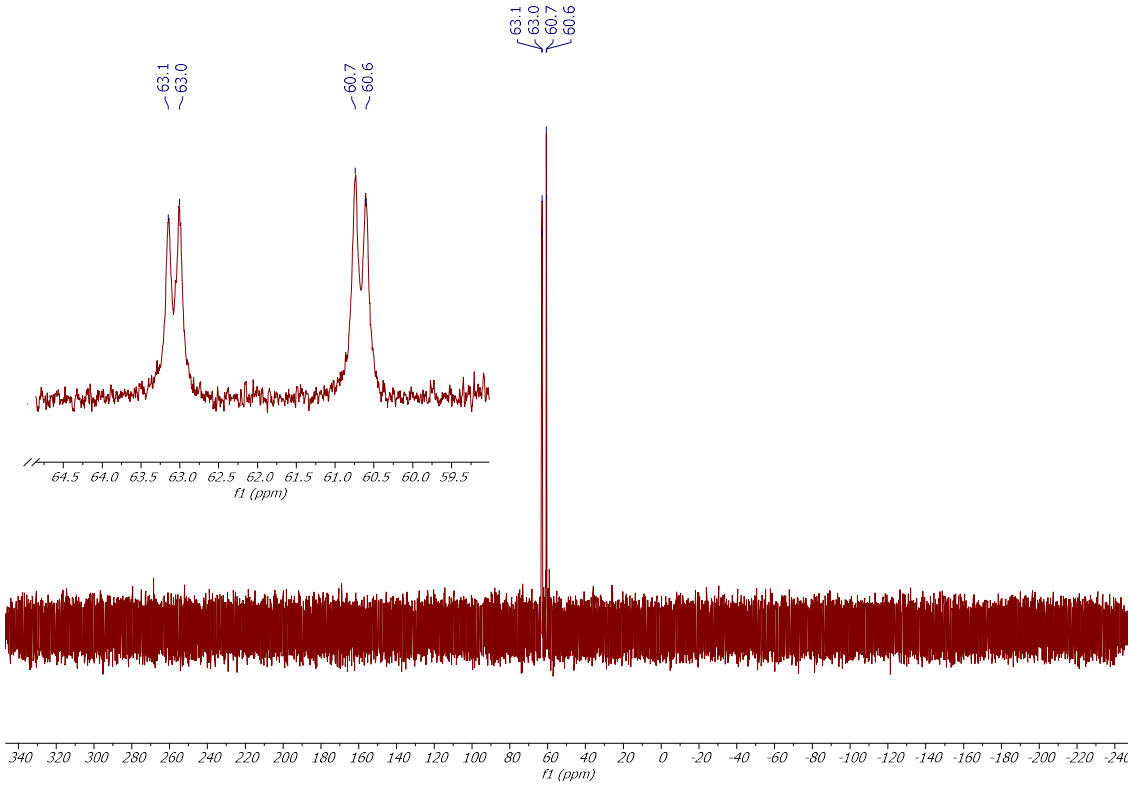

Figure 15: $^{31}P\{^{1}H\}$ NMR spectrum (162 MHz, CD_3OD, 298K) of **7**.

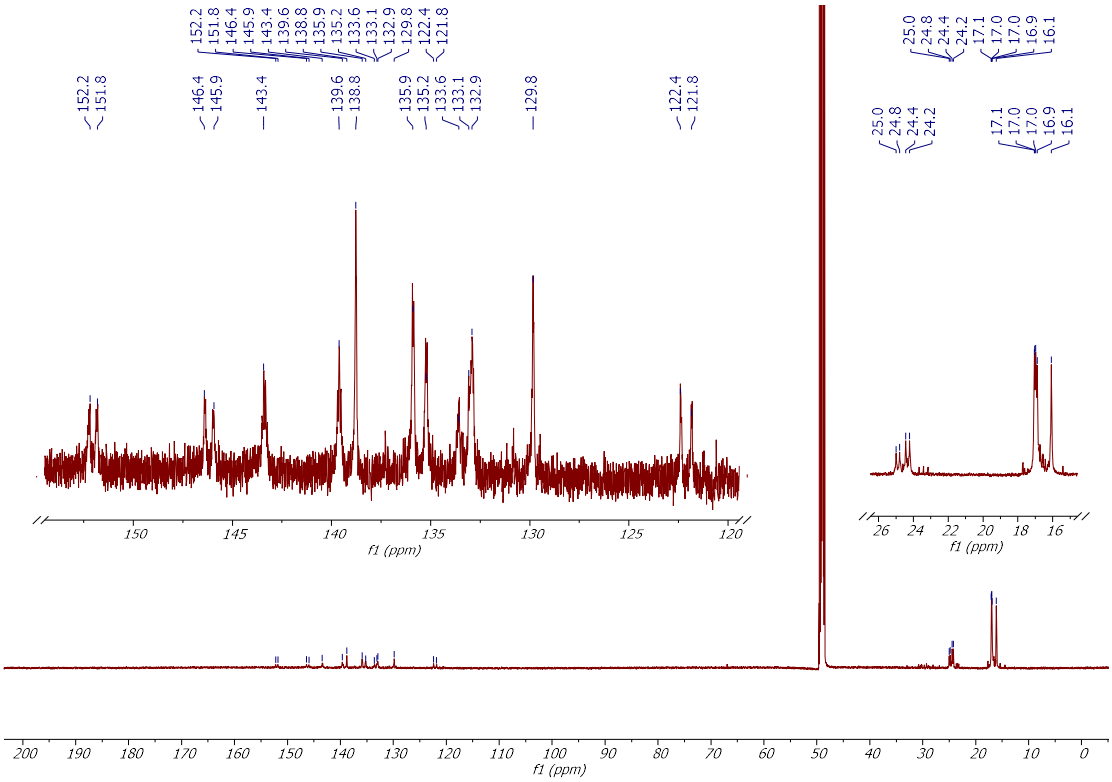

Figure 16: ^{13}C NMR spectrum (151 MHz, CD_3OD, 298K) of **7**.

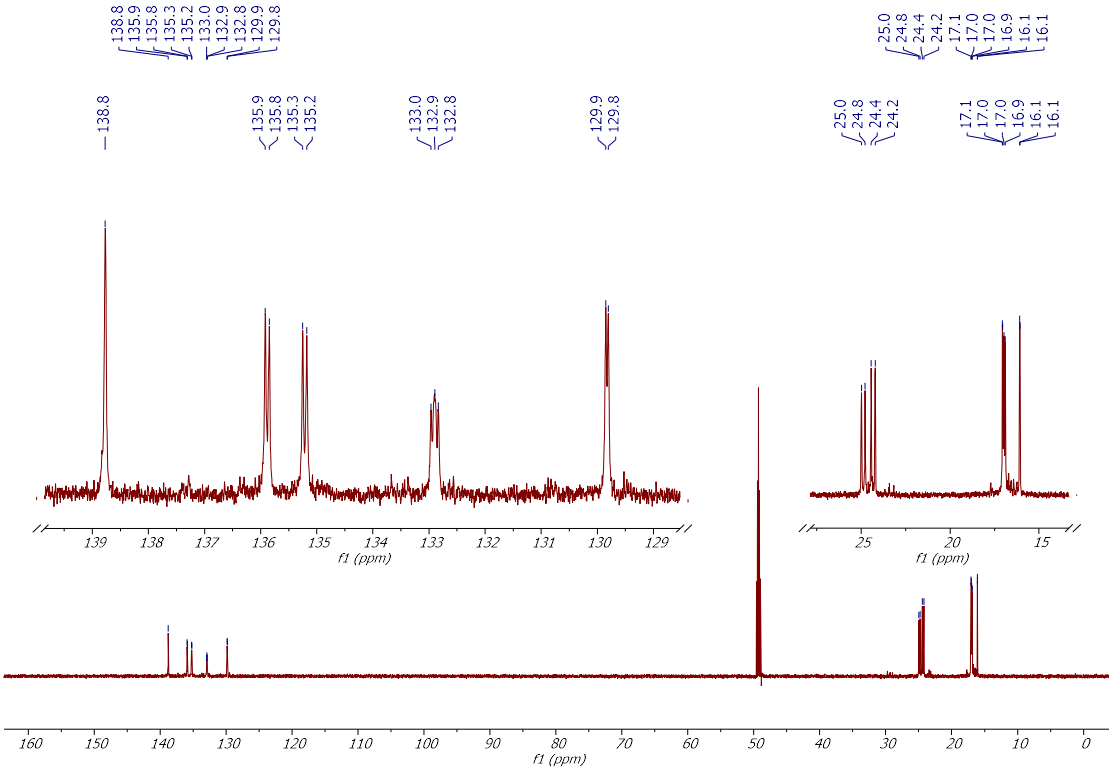

Figure 17: ^{13}C dept-135 NMR spectrum (151 MHz, CD_3OD, 298K) of **7**.

[PhPhPh]Cl. Inside the glovebox compound **5** (10.0 mg, 13.5 µmol) was dissolved in dry CH_2Cl_2 (0.5 mL) in a *J*-Young NMR tube. FcCl (2.98 mg, 13.5 µmol, 1.00 eq) was added. After 5 min, the formation of an EPR signal was observed. **MALDI HR-MS** (pos): *m/z* calcd for $C_{46}H_{66}P_4^+$ $[M]^+$ 742.4110, found 742.4112. *Due to its low stability, the product could only be observed in-situ by EPR and mass spectrometry. In addition to the expected signal, the mass spectra show features attributable to other oxidation states, likely arising from partial decomposition during the measurement.*

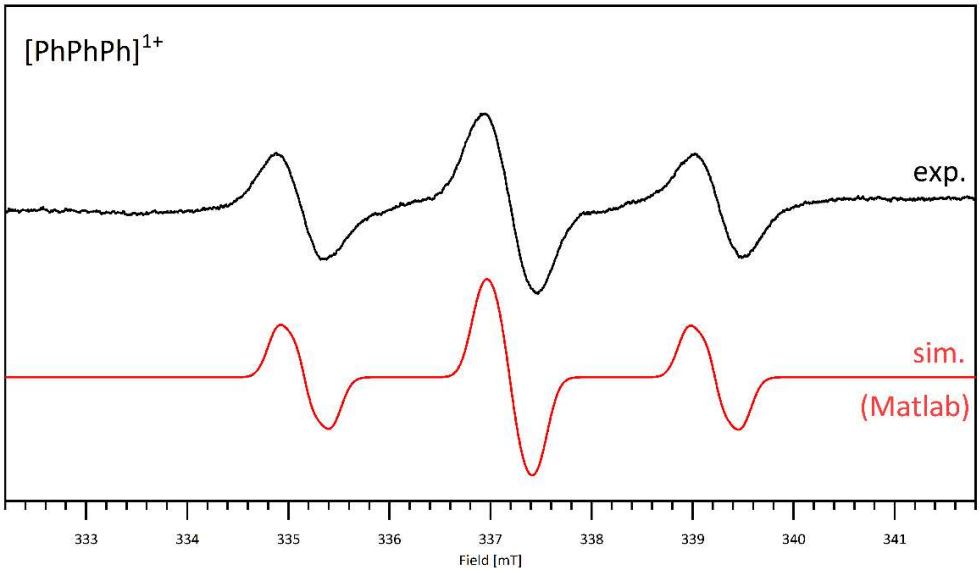

Figure 18: Experimental (ν = 9.443296 GHz, g_{iso} = 2.0012) and the simulated EPR spectrum for [**PhPhPh**]$^{1+}$ (fitting parameters: g_{iso} = 2.0022; $A_{iso1,sim}(^{31}P)$ = -58.2756 MHz; $A_{iso2,sim}(^{31}P)$ = -55.4521 MHz; $A_{iso3,sim}(^{31}P)$ = 4.3381 MHz; $A_{iso4,sim}(^{31}P)$ = 6.0927 MHz). Simulations were performed using EasySpin v6.0.9 and Matlab R2025a.[1-3] A comparison with the computed EPR spectra is provided in Section EPR: Computational Modeling. **Considering the discrepancy observed in Figure 46 and the overall good agreement in Figure 45 (see Section EPR: Computational Modeling), it can be concluded that the experimental spectrum of [PhPhPh]$^{1+}$ is more consistent with a one-side-cyclized structure rather than a two-side-cyclized structure.**

[**PhPhPh**]**Cl$_3$**. Inside the glovebox compound **5** (5.60 mg, 7.54 µmol) was dissolved in dry CH_2Cl_2 (0.5 mL) in a *J*-Young NMR tube. Ph_3CCl (6.30 mg, 22.6 µmol, 3.00 eq) was added and the mixture was stirred at rt on an orbital-stirrer for 16 h. The solvent was removed under reduced pressure, and the crude product was washed with toluene and thf. A deep green solid was obtained. An EPR signal was observed, but compound [**PhPhPh**]**Cl$_3$** could not be isolated. **MALDI HR-MS** (pos): *m/z* calcd for $C_{46}H_{66}P_4Cl_2^+$ [M+2Cl]$^+$ 812.3487, found 812.3518; calcd for $C_{46}H_{66}P_4BrCl^+$ [M+Br+Cl]$^+$ 856.2988, found 856.3018; $C_{46}H_{66}P_4Br_2^+$ [M+2Br]$^+$ 900.2476, found 900.2503. *Due to its low stability, the product could only be observed in-situ by EPR and mass spectrometry. In addition to the expected signal, the mass spectra show features attributable to other oxidation states, likely arising from partial decomposition during the measurement.*

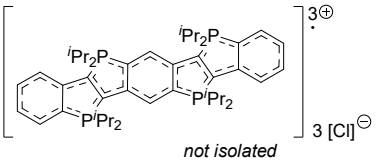

not isolated

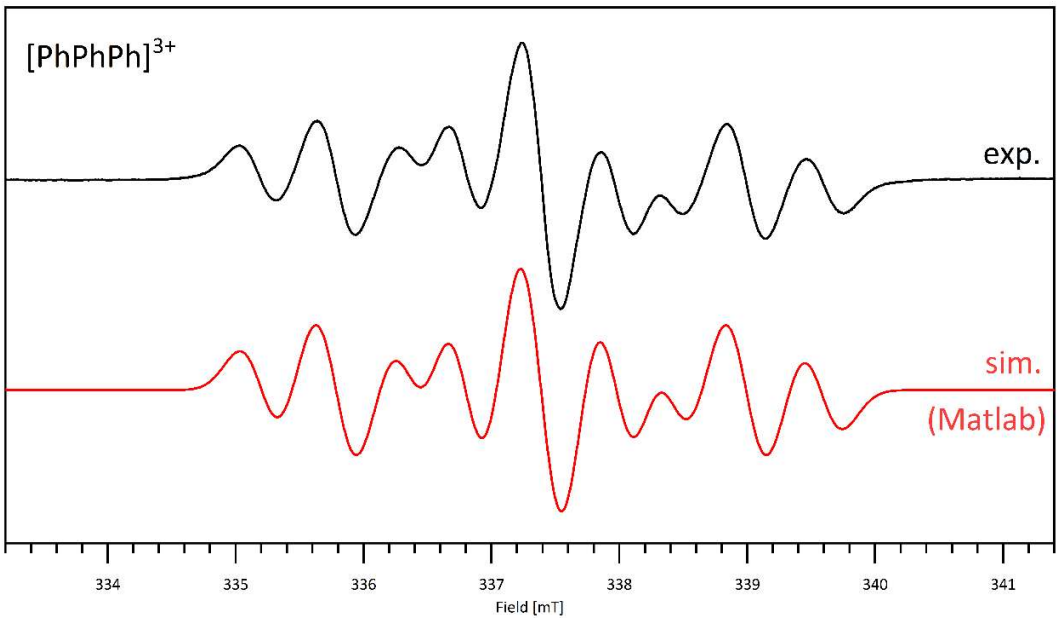

Figure 19: Experimental (ν = 9.449465 GHz, g_{iso} = 2.0013) and the simulated EPR spectrum for [**PhPhPh**]$^{3+}$ in CH_2Cl_2 at rt (fitting parameters: g_{iso} = 2.0011; $A_{iso1,sim}(^{31}P)$ = -17.6844 MHz; $A_{iso2,sim}(^{31}P)$ = -43.7523 MHz; $A_{iso3,sim}(^{31}P)$ = -46.0084 MHz; $A_{iso4,sim}(^{31}P)$ = -15.0754 MHz). Simulations were performed using EasySpin v6.0.9 and Matlab R2025a.[1-3] A comparison with the computed EPR spectra is provided in Section EPR: Computational Modeling.

(2,5-bis((3-(diisopropylphosphaneyl)naphthalen-2-yl)ethynyl)-1,4-phenylene)bis(diisopropyl-phosphane). In a flame-dried and argon-filled ampulla compound **4** (600 mg, 864 µmol) was dissolved in dry thf (40 mL). A 1.7 M solution of *t*-BuLi in hexanes (4.07 ml, 6.92 mmol, 8.00 eq.) was added dropwise at –78 °C. The mixture was stirred for 2.0 h at this temperature and $^{i}Pr_2PCl$ (792 mg, 825 µL, 5.19 mmol, 6.00 eq) was added dropwise. The reaction mixture was stirred in cryostat at –8 °C for 16 h. Conversion was confirmed via ^{31}P NMR spectroscopy, and the solvent was removed under reduced pressure. Inside the glovebox the crude mixture was suspended in toluene and filtered over Celite. Recrystallization from dry toluene (–40 °C) afforded compound **6** as off-white solid (513 mg, 70%). **MP**: 112 °C (decomp.). **ATR-IR** (selected peaks): ν [cm^{-1}] = 2952, 2922, 2896, 2866, 1457, 1383, 1360, 1148, 1036, 1018, 891, 880, 749, 731, 693, 667. **^{1}H NMR** (600 MHz, thf-d_8): δ (in ppm) = 8.19 (d, J_{H-P} = 2.3 Hz, 2H), 8.06 (d, J_{H-P} = 5.7 Hz, 2H), 7.98–7.97 (m, 2H), 7.90–7.88 (m, 4H), 7.53–7.50 (m, 4H), 2.58–2.53 (m, 4H), 2.40–2.35 (m, 4H), 1.25–1.21 (m, 24H), 1.09–1.06 (m, 12H), 1.02–0.99 (m, 12H). **^{31}P {^{1}H} NMR** (162 MHz, thf-d_8): δ (in ppm) = 10.0 (s, 2P), 4.0 (s, 2P). **^{13}C {^{1}H} NMR** (151 MHz, thf-d_8): δ (in ppm) = 139.4 (d, J_{C-P} = 25.5 Hz, C_q, 2C), 138.2 (CH, 2C), 136.3 (d, J_{C-P} = 23.7 Hz, C_q, 2C), 135.7 (CH, 2C), 134.1 (C_q, 2C), 133.5 (d, J_{C-P} = 5.1 Hz, C_q, 2C), 133.2 (d, J_{C-P} = 3.5 Hz, CH, 2C), 130.7 (d, J_{C-P} = 28.3 Hz, C_q, 2C), 128.8 (CH, 2C), 128.3 (CH, 2C), 128.0 (CH, 2C), 127.8 (CH, 2C), 127.2 (d, J_{C-P} = 21.2 Hz, C_q, 2C), 97.9–97.8 (m, C_q, 2C), 95.2–95.2 (m, C_q, 2C), 24.8– 24.7 (d, J_{C-P} = 14.3 Hz, CH, 4C), 24.5 (d, J_{C-P} = 15.2 Hz, CH, 4C), 21.0 (d, J_{C-P} = 19.8 Hz, CH_3, 4C), 20.5 (d, J_{C-P} = 18.5 Hz, CH_3, 4C), 20.4 (d, J_{C-P} = 12.0 Hz, CH_3, 4C),

20.0 (d, $J_{C\text{-}P}$ = 11.0 Hz, CH_3, 4C). **Anal. Calcd. for** $C_{54}H_{70}P_4$ (843.0 g/mol): C 76.93, H 8.37. Found: C 77.01, H 8.43. **LIFDI** (pos): *m/z* calcd for $C_{54}H_{70}P_4^+$ $[M]^+$ 842.4423, found 842.4942.

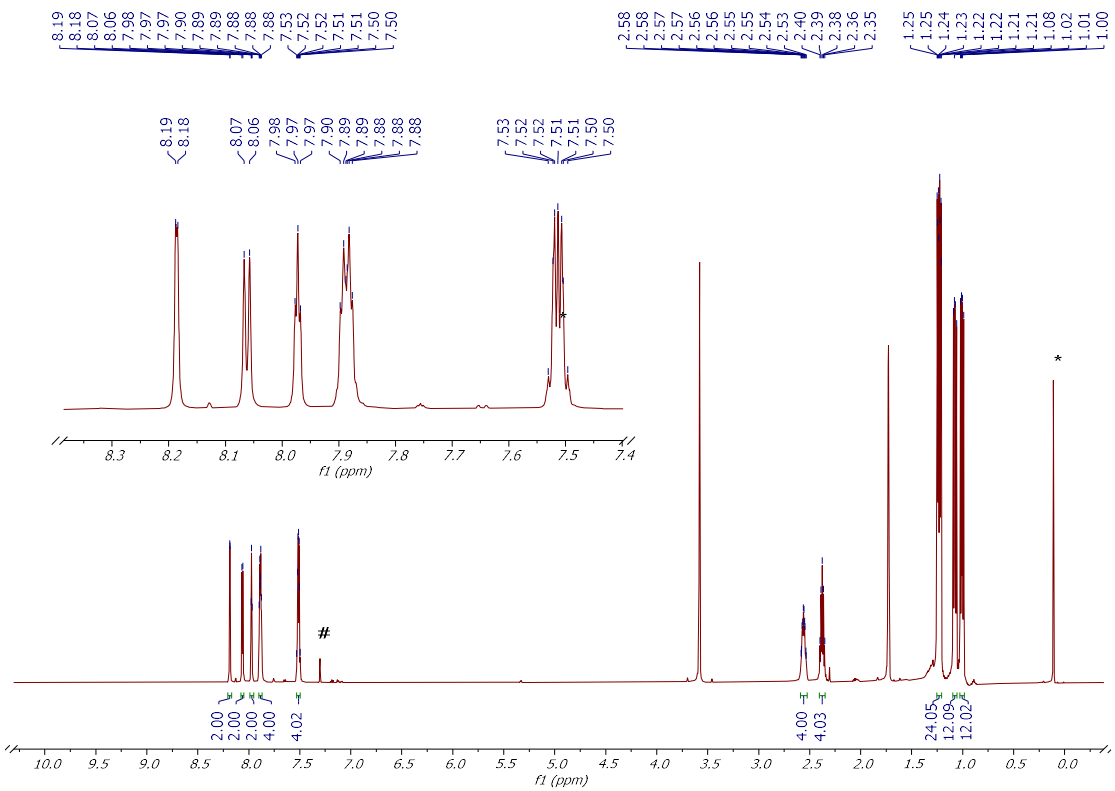

Figure 20: **^{1}H NMR** spectrum (600 MHz, thf-d_8, 298K) of **6** (traces of impurities of benzene (#) and silicon grease (*) are marked).

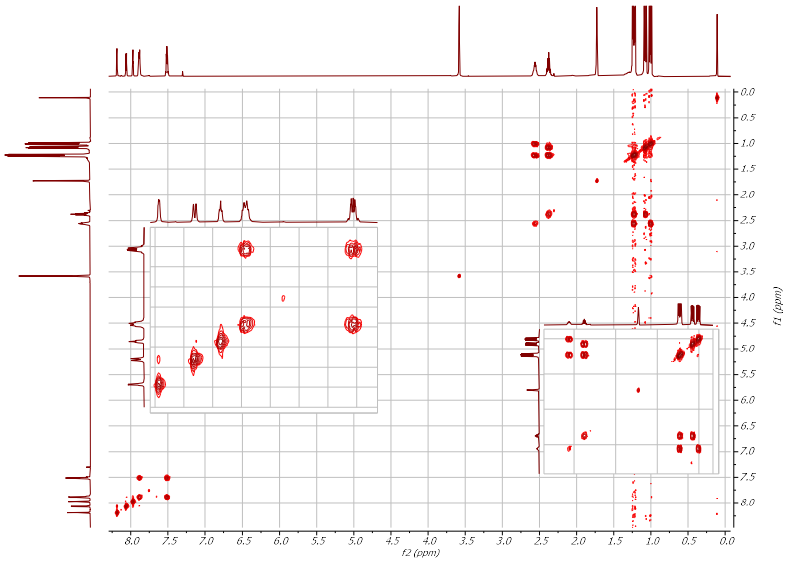

Figure 21: **^{1}H^{1}H-Cosy NMR** spectrum (600 MHz, thf-d_8, 298K) of **6**.

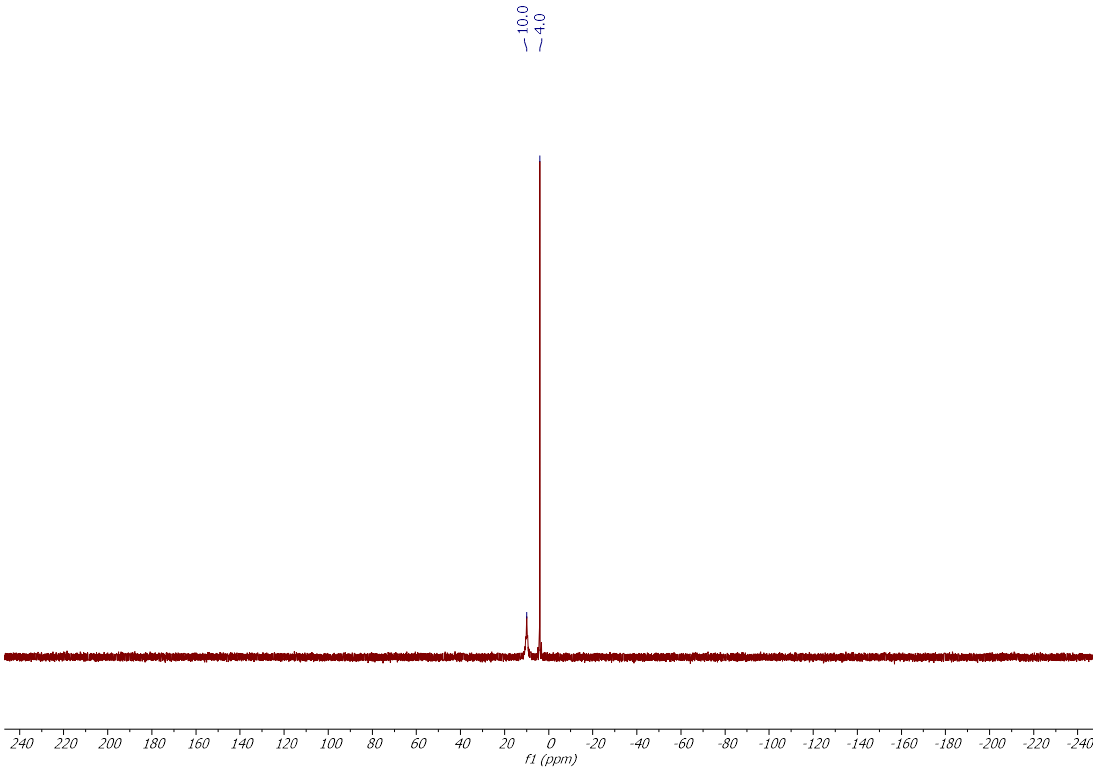

Figure 22: $^{31}P\{^{1}H\}$ **NMR** spectrum (162 MHz, thf-d_8, 298K) of **6**.

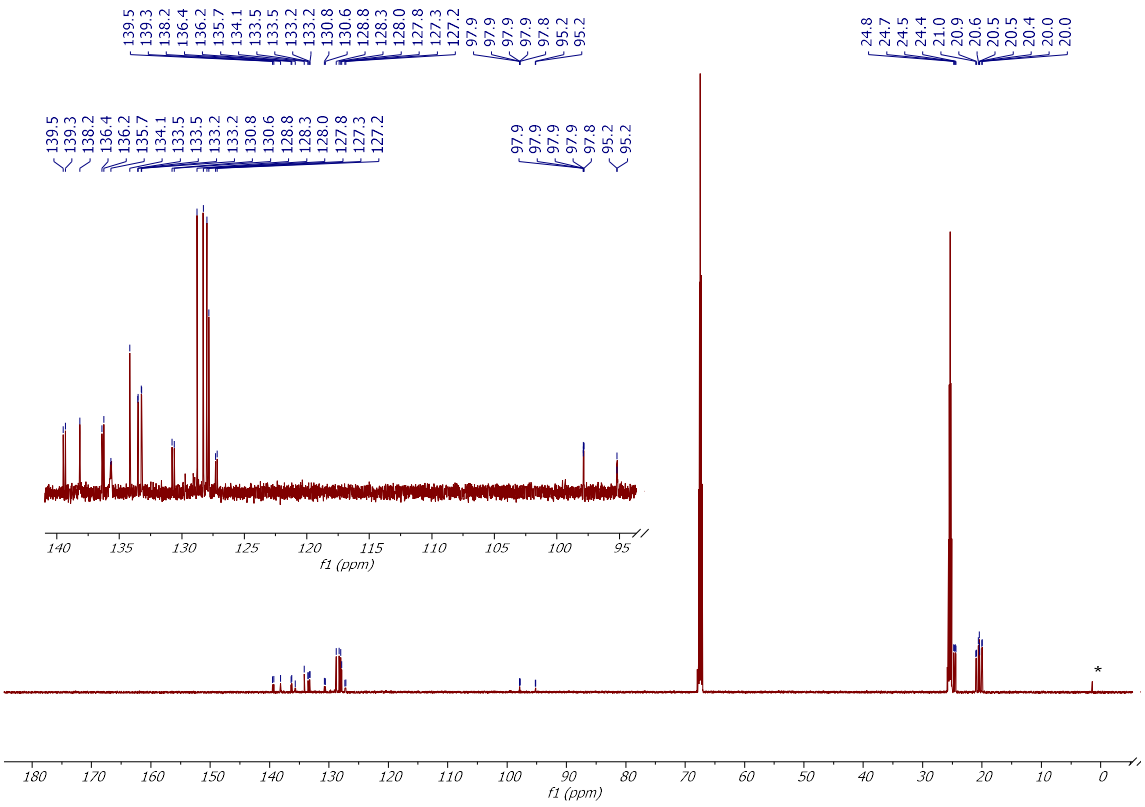

Figure 23: $^{13}C\{^{1}H\}$ **NMR** spectrum (151 MHz, thf-d_8, 298K) of **6** (traces of impurities of silicon grease (*) are marked).

[NapPhNap]Br$_4$ (8). Inside the glovebox compound **6** (100 mg, 119 µmol) was dissolved in dry

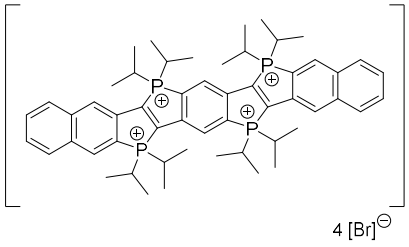

CH_2Cl_2 (10 mL) at –40 °C. $C_2Cl_4Br_2$ (39.4 mg, 121 µmol, 1.02 eq.) was added and the mixture was warmed to rt over 30 min. Further $C_2Cl_4Br_2$ (39.4 mg, 121 µmol, 1.02 eq.) was added and the mixture was stirred at rt for 16 h. Conversion was confirmed via ^{31}P NMR spectroscopy. Pentane (10 mL) was added and the mixture was filtered. Recrystallization from MeOH/Et_2O afforded compound **8** as deep red solid (84.0 mg, 61%). **MP**: 198 °C (decomp.). **ATR-IR** (selected peaks): ν [cm^{-1}] = 2971, 2822, 1461, 1439, 1372, 1267, 1215, 1155, 1085, 1040, 921, 906, 880, 760, 738, 708, 690, 667. **^{1}H NMR** (600 MHz, CD_3OD): *δ* (in ppm) = 9.40 (d, J_{H-P} = 8.7 Hz, 1H), 9.07 (d, J_{H-P} = 10.3 Hz, 1H), 8.73 (d, J_{H-P} = 3.4 Hz, 1H), 8.38 (d, J_{H-P} = 7.7 Hz, 1H), 8.33 (d, J_{H-P} = 7.6 Hz, 1H), 8.02–7.98 (m, 4H), 4.76–4.70 (m, 4H), 4.57–4.51 (m, 4H), 1.69–1.60 (m, 36H), 1.49–1.45 (m, 12H). **^{31}P {^{1}H} NMR** (243 MHz, CD_3OD): *δ* (in ppm) = 62.8 (d, J_{P-P} = 21.9 Hz, 2P), 58.2 (d, J_{C-P} = 21.9 Hz, 2P). **^{13}C {^{1}H} NMR** (151 MHz, CD_3OD): *δ* (in ppm) = 152.3–151.9 (m, C_q, 2C), 144.6–144.1 (m, C_q, 2C), 143.7–143.5 (m, C_q, 2C), 139.8 (d, J_{C-P} = 10.3 Hz, CH, 2C), 137.2 (d, J_{C-P} = 1.4 Hz, C_q, 2C), 135.2 (d, J_{C-P} = 12.6 Hz, C_q, 2C), 134.5–134.4 (m, C_q, 2C), 133.2 (CH, 2C), 132.7 (bs, CH, 4C), 131.8, (CH, 2C), 131.5 (CH, 2C), 131.5 (CH, 2C). **MALDI HR-MS** (pos): *m/z* calcd for $C_{54}H_{70}P_4Br_3^+$ [M+3Br]$^+$ 1079.1973, found 1079.1972.

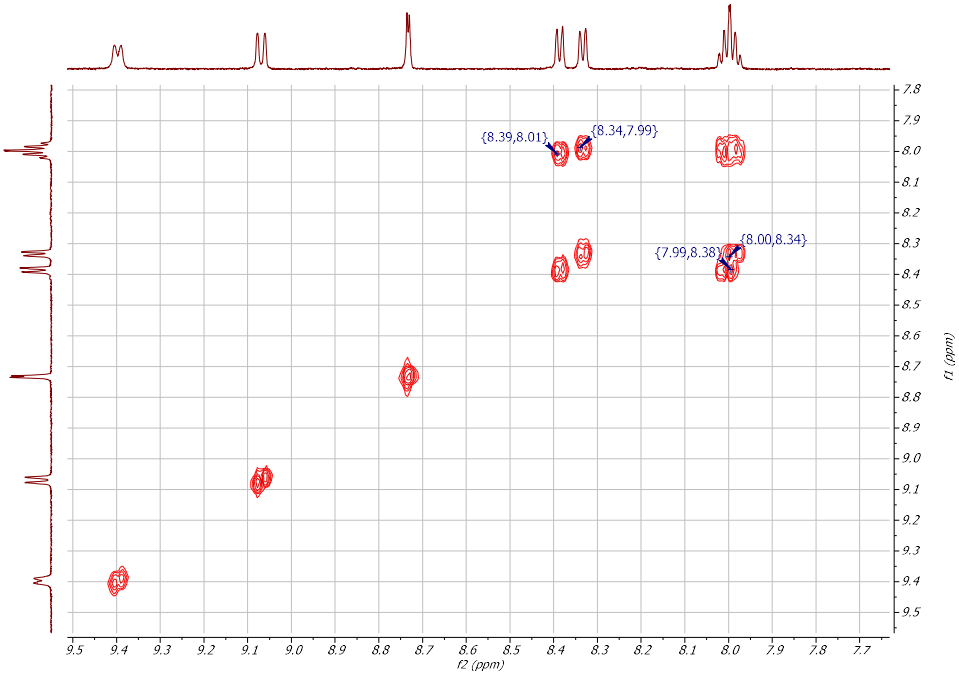

Figure 24: ^{1}H^{1}H-Cosy NMR spectrum (600 MHz, CD_3OD, 298K) of **8**.

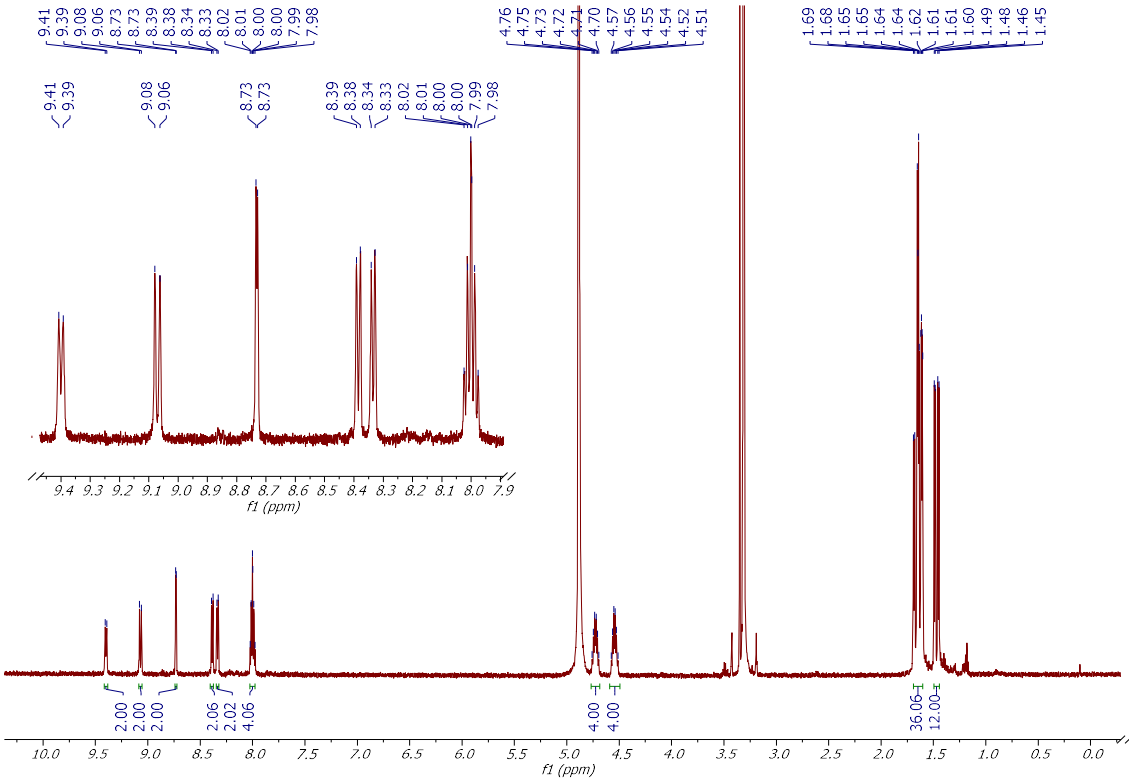

Figure 25: ^{1}H NMR spectrum (600 MHz, CD_3OD, 298K) of **8**.

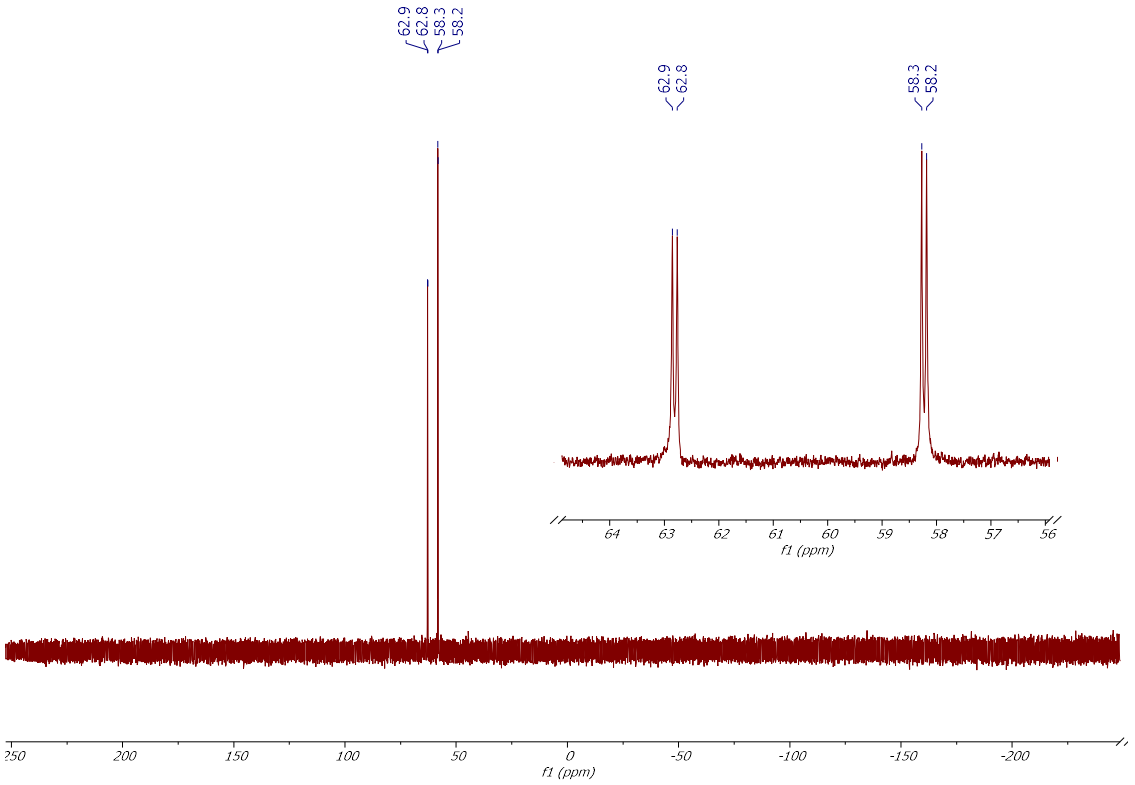

Figure 26: ^{31}P NMR spectrum (243 MHz, CD_3OD, 298K) of **8**.

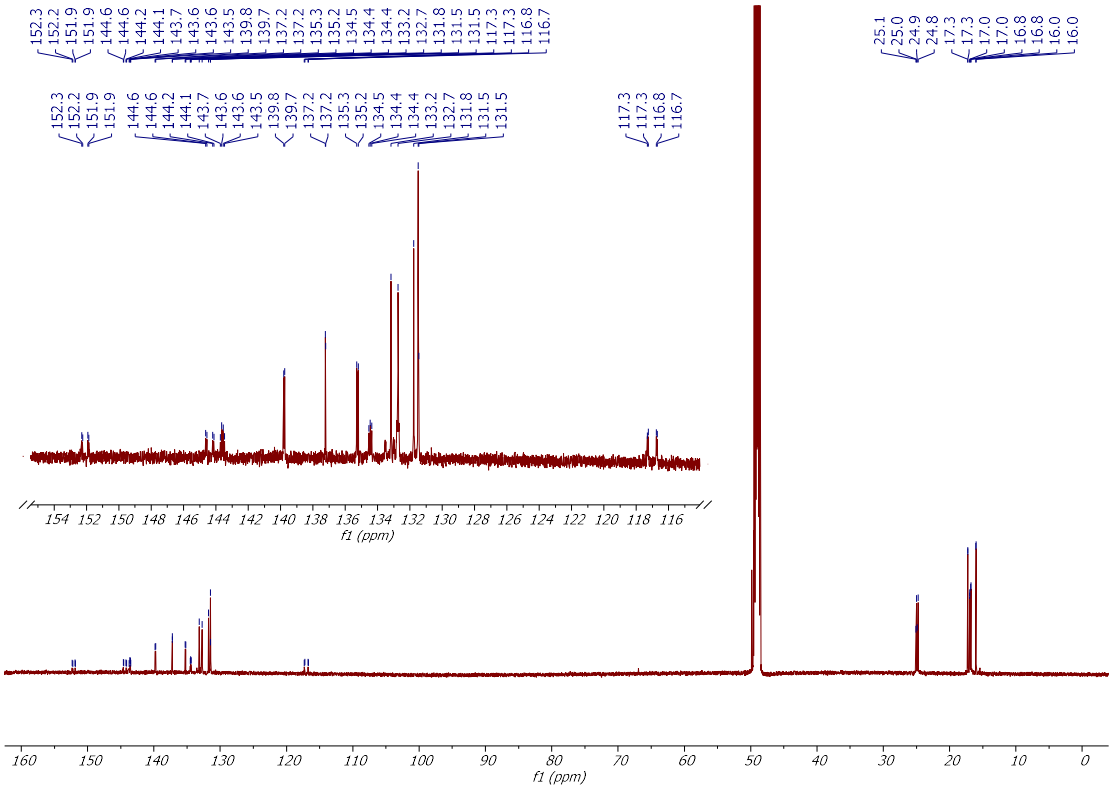

Figure 27: ^{13}C NMR spectrum (151 MHz, CD_3OD, 298K) of **8**.

3) Absorption and Emission Spectra

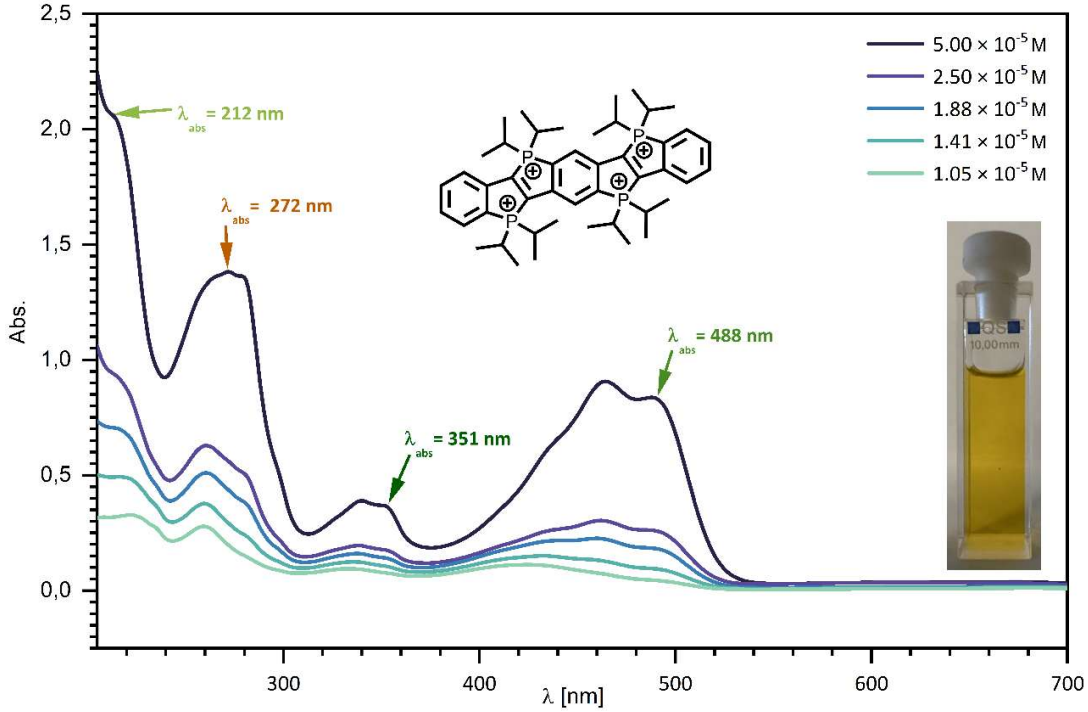

Figure 28: Concentration dependent UV-Vis spectra of **7** in MeOH at rt.

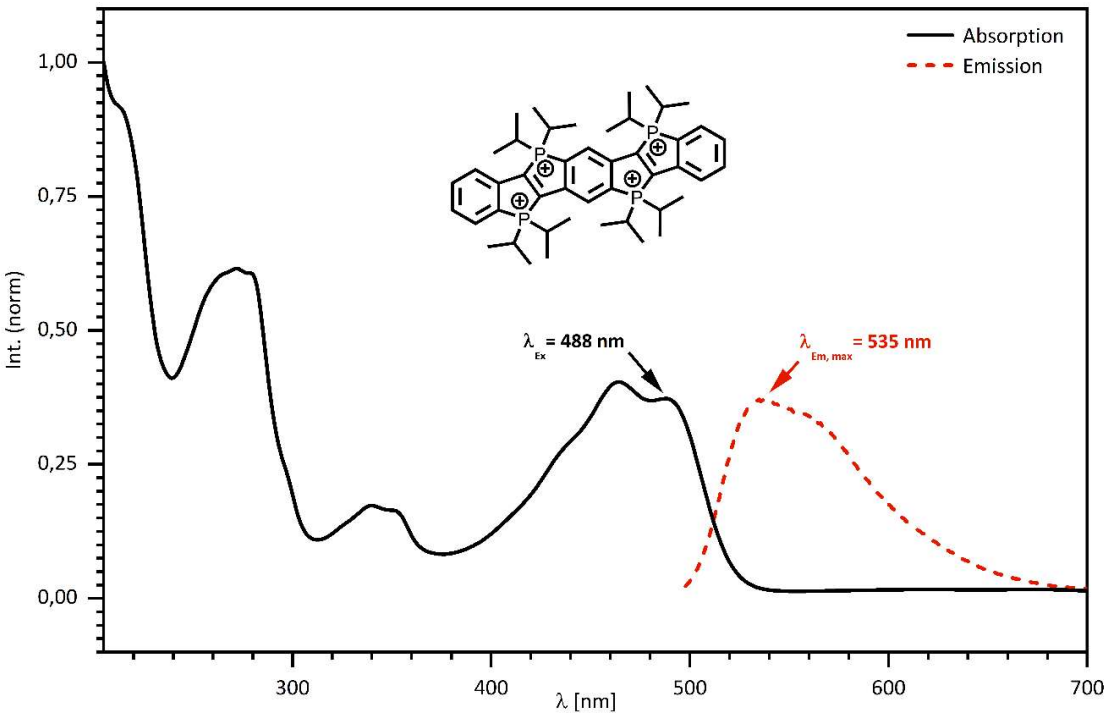

Figure 29: Absorption and emission spectra of **7** in MeOH at rt ($\lambda_{Exitation}$ = 488 nm, 5.00 × 10^{-5} M).

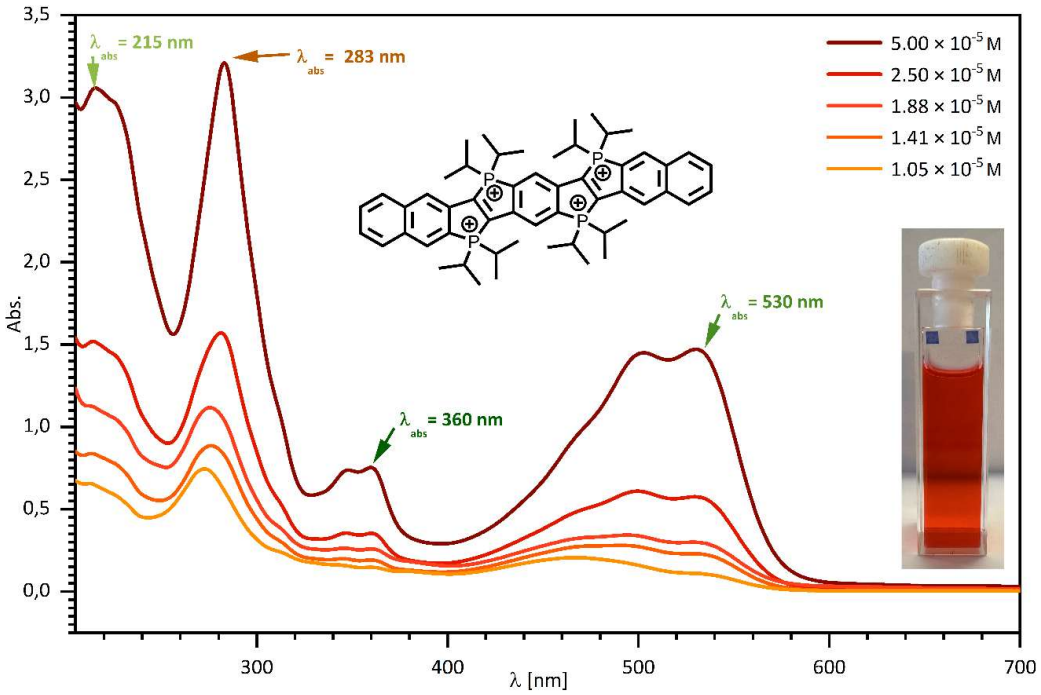

Figure 30: Concentration dependent UV-Vis spectra of **8** in MeOH at rt.

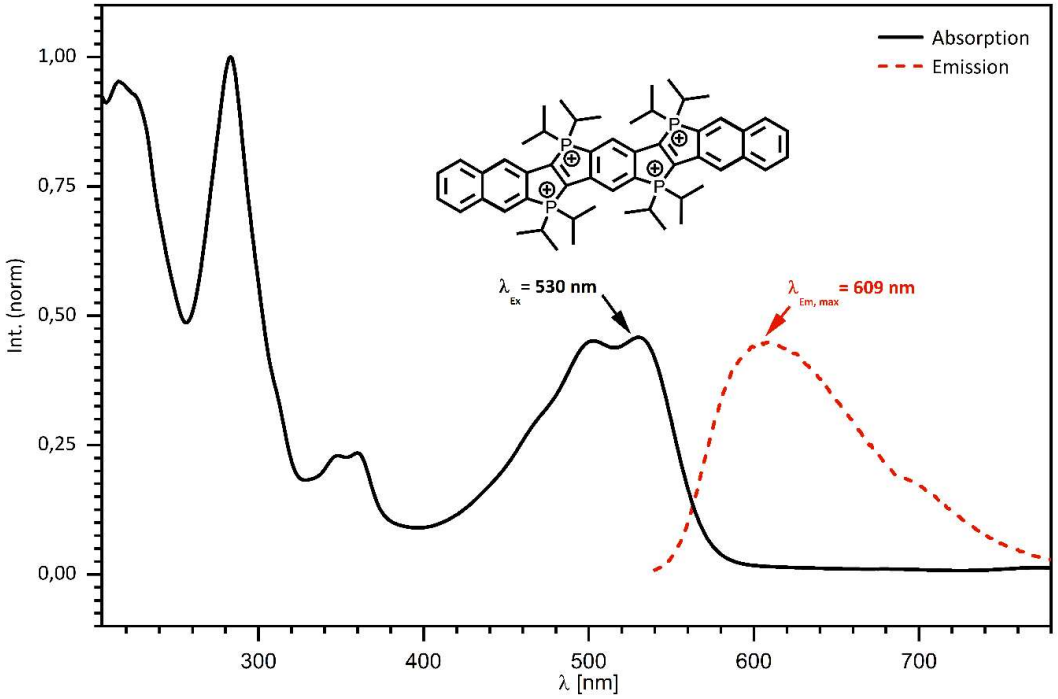

Figure 31: Absorption and emission spectra of **8** in MeOH at rt ($\lambda_{Exitation}$ = 530 nm, 5.00 × 10^{-5} M).

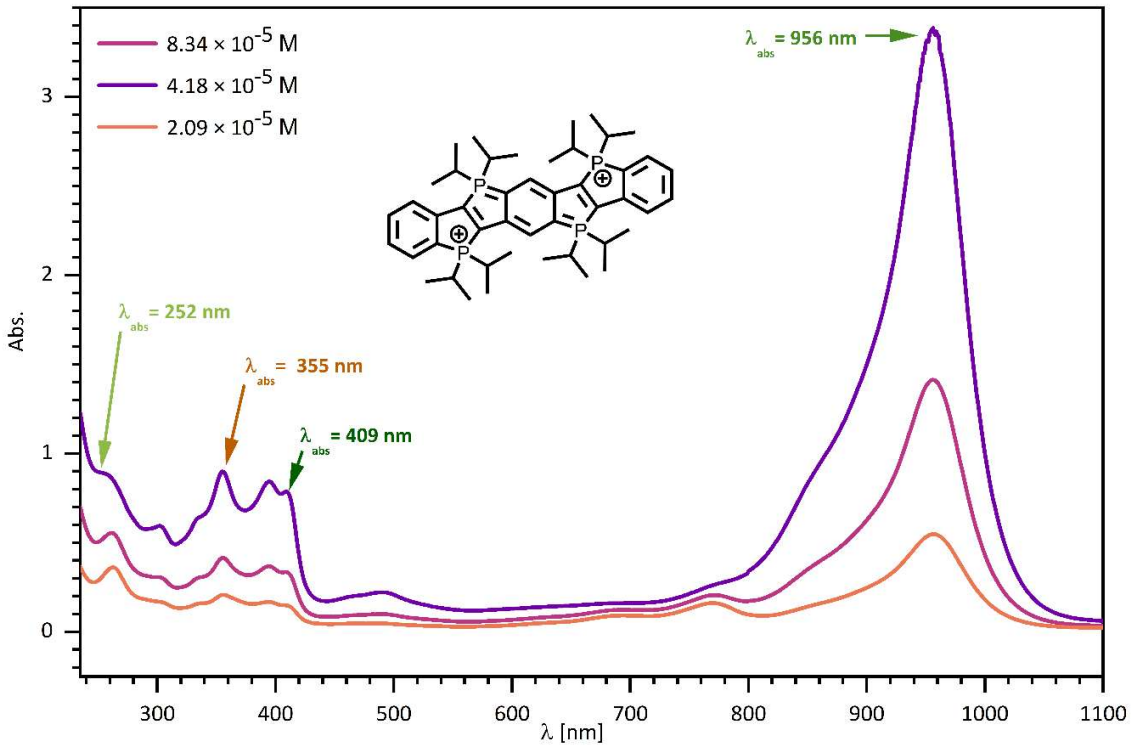

Figure 32: Concentration dependent UV-Vis spectra of **9** in CH_2Cl_2 at rt under argon atmosphere.

Table 1: Summery of optical data. Molar absorption coefficients from fitting (see (4) Molar Extinction Coefficients) are shown for different wavelengths with the respective errors from the linear fits.

compound	**7***	**8***	**9****
ε / 10^3 $M^{-1}s^{-1}$ (λ / nm)	44.0 ± 0.5 (212 nm)	61.5 ± 0.5 (215 nm)	9.5 ± 0.2 (252 nm)
ε / 10^3 $M^{-1}s^{-1}$ (λ / nm)	30.1 ± 1.1 (272 nm)	66.6 ± 1.8 (283 nm)	11.1 ± 0.4 (355 nm)
ε / 10^3 $M^{-1}s^{-1}$ (λ / nm)	7.3 ± 0.2 (351 nm)	15.5 ± 0.3 (360 nm)	10.3 ± 0.5 (409 nm)
ε / 10^3 $M^{-1}s^{-1}$ (λ / nm)	20.3 ± 1.1 (488 nm)	34.9 ± 1.5 (530 nm)	45.7 ± 1.5 (956 nm)
$\lambda_{Emission}$ ($\lambda_{Excitation}$)	535 nm (488 nm)	609 nm (530 nm)	-

*Absorption and emission measurements for compounds **7** and **8** were carried out in methanol.
Absorption measurements for compound **9 were carried out in CH_2Cl_2 under argon atmosphere due to its high reactivity. This compound does not show fluorescence.

4) Molar Extinction Coefficients

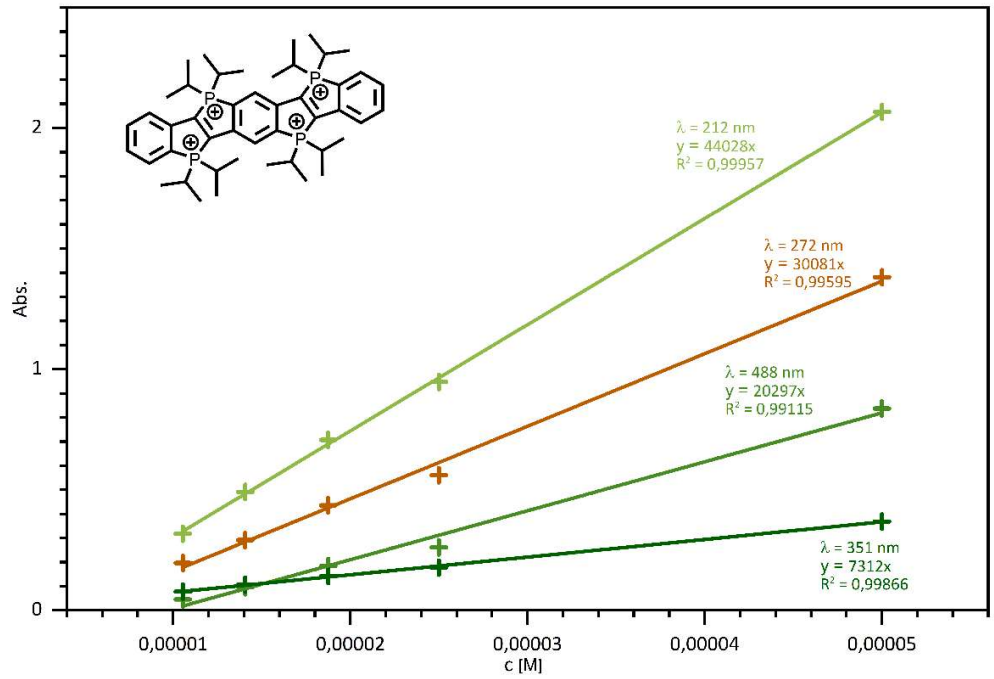

Figure 33: Determination of molar extinction coefficient for different wavelengths of **7**.

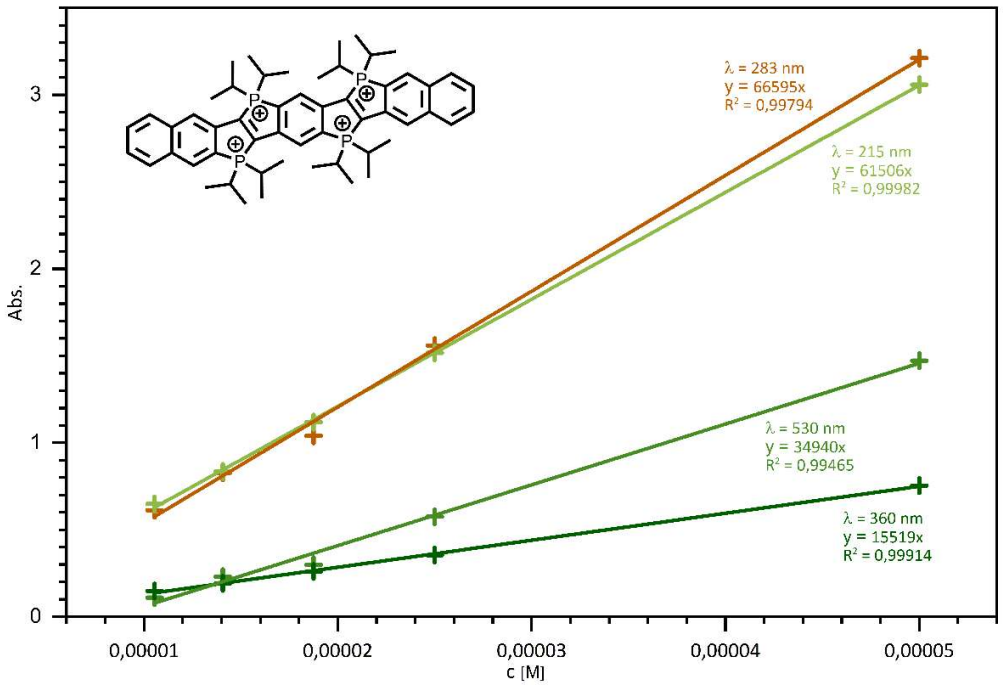

Figure 34: Determination of molar extinction coefficient for different wavelengths of **8**.

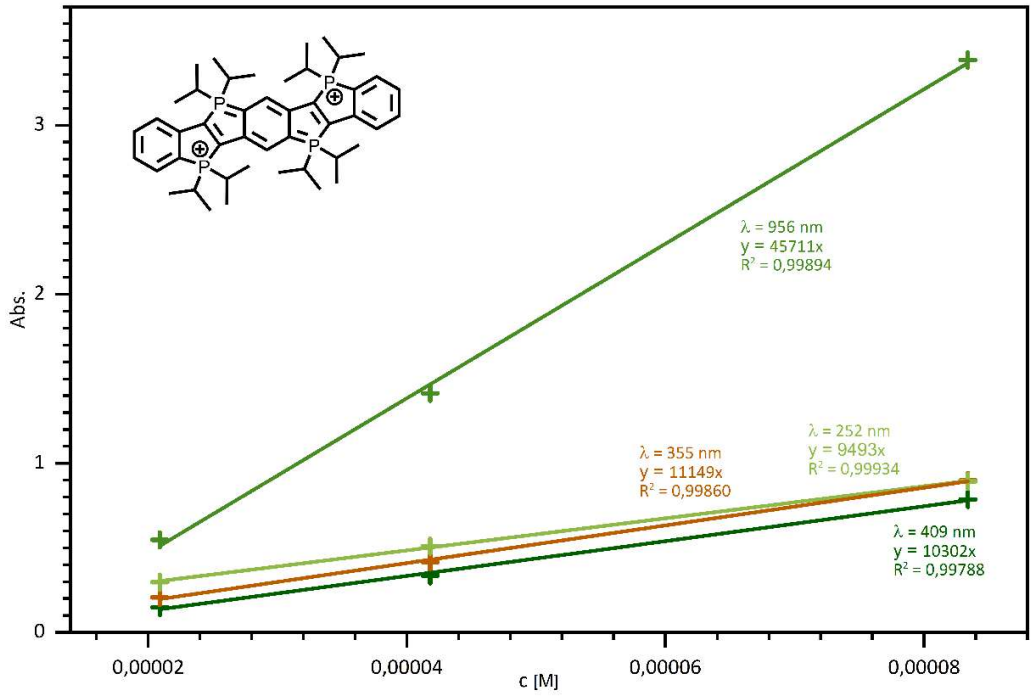

Figure 35: Determination of molar extinction coefficient for different wavelengths of **9**.

5) Cyclic Voltammograms

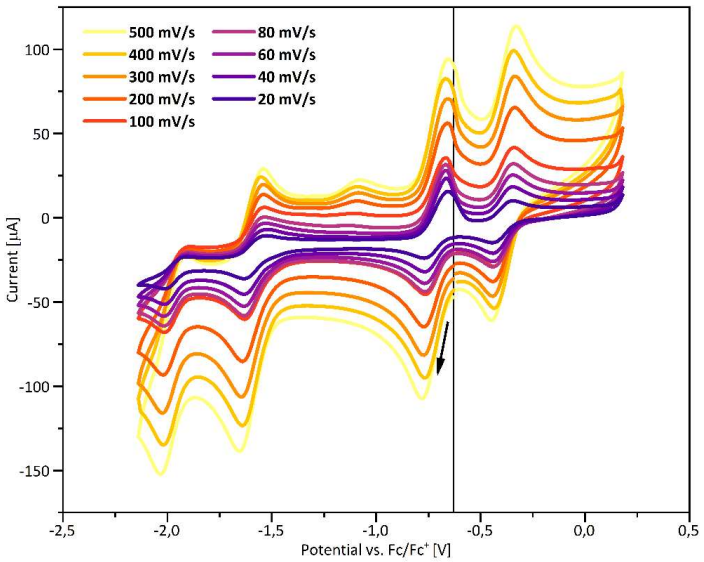

Figure 36a: Cyclic voltammograms of **7** in MeCN, supp. electrolyte Bu_4NOTf (0.1 M), reference Fc/Fc^+.

Table 2: Summery of electrochemical data. Redox potentials for **7** are given vs. Fc/Fc^+. All measurements were conducted in MeCN/NBu_4OTf (0.1 M).

E (V)	reversibility	assigned redox process
$E_{1/2}$ = –0.39 V	quasi reversible	$[PhPhPh]^{4+} + e^- \rightleftharpoons [PhPhPh]^{3+}$
$E_{1/2}$ = –0.72 V	quasi reversible	$[PhPhPh]^{3+} + e^- \rightleftharpoons [PhPhPh]^{2+}$
$E_{1/2}$ = –1.58 V	quasi reversible	$[PhPhPh]^{2+} + e^- \rightleftharpoons [PhPhPh]^{1+}$
E = –2.02 V	irreversible	$[PhPhPh]^{1+} + e^- \rightarrow [PhPhPh]^{0}$ *

*Irreversibility might be explained by decomposition of $[PhPhPh]^0$. This is in accordance with experimental observation of the formation of **10**, whereas the corresponding doubly cyclized P-diylide was not detected.

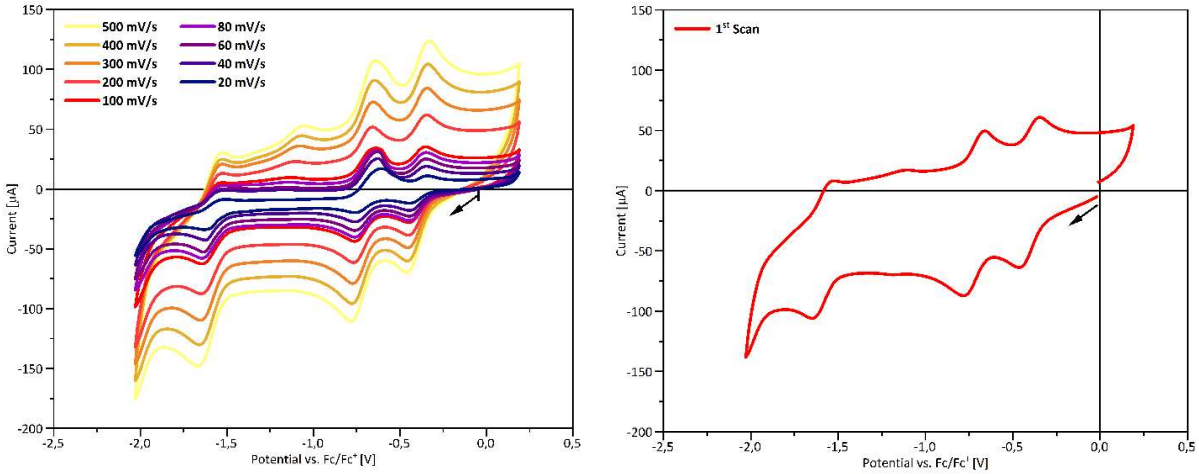

Figure 36b: Cyclic voltammograms of **7** in MeCN, supp. electrolyte Bu_4NOTf (0.1 M), reference Fc/Fc^+. Initiation at 0 V vs. Fc/Fc^+ and observing no current at the starting potential implies that the redox process at $E_{1/2}$ = –0.39 V can be assinged to the first reduction process.

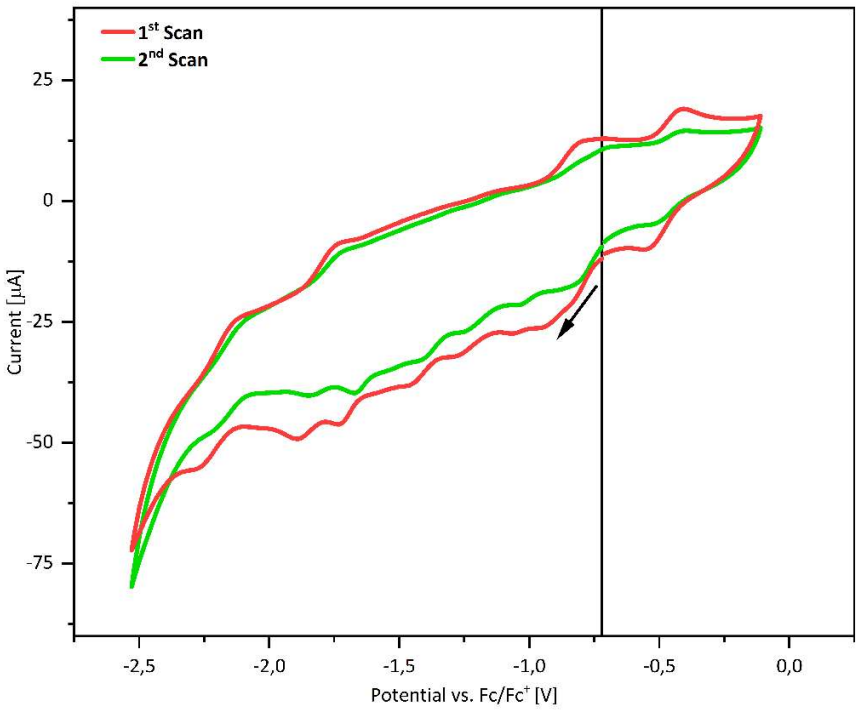

Figure 37: Cyclic voltammograms of **8** in MeCN, supp. electrolyte Bu_4NOTf (0.1 M), reference Fc/Fc^+.

6) ATR-IR Spectra

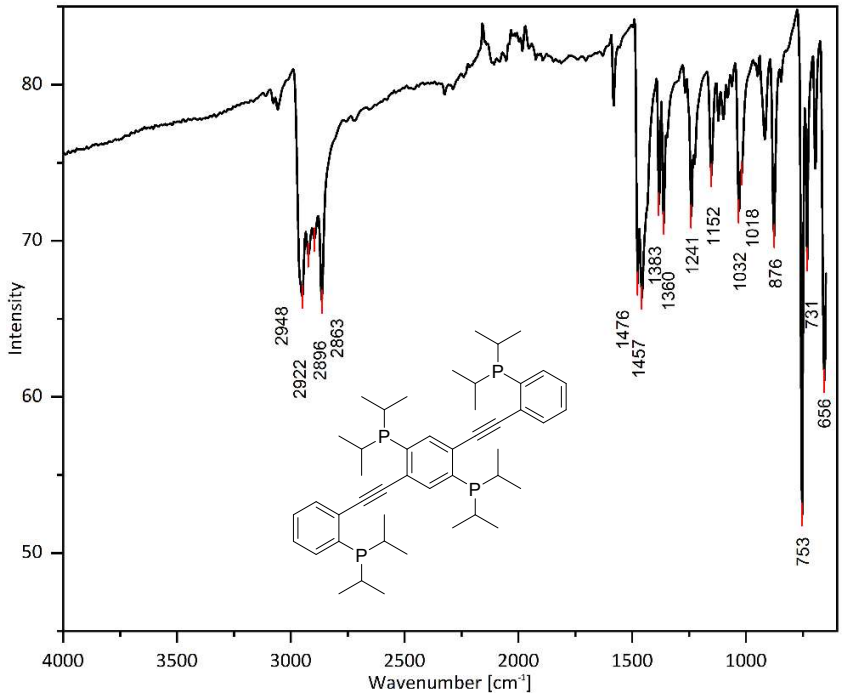

Figure 38: ATR-IR spectrum of **5** at rt under argon.

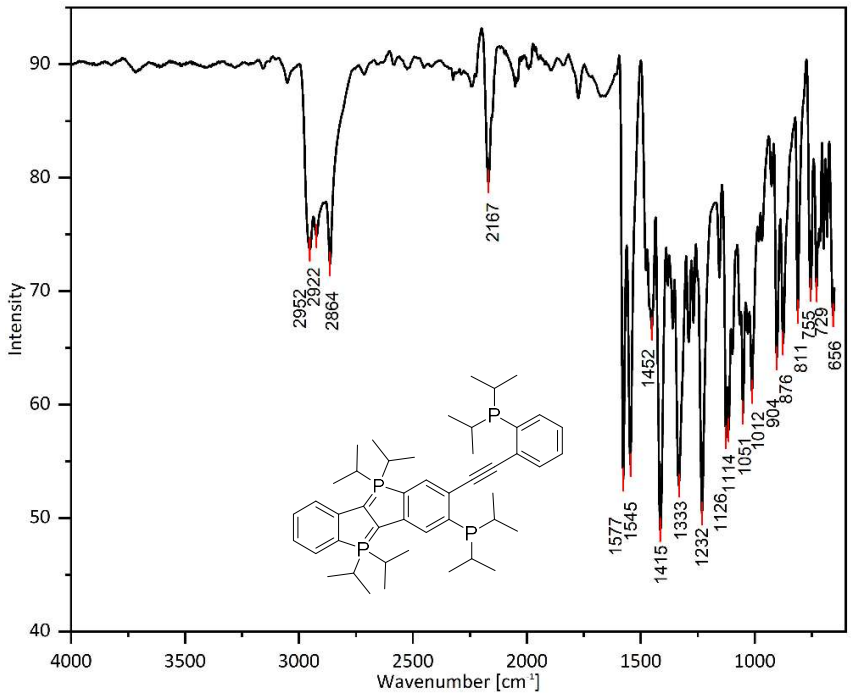

Figure 39: ATR-IR spectrum of **10** at rt under argon.

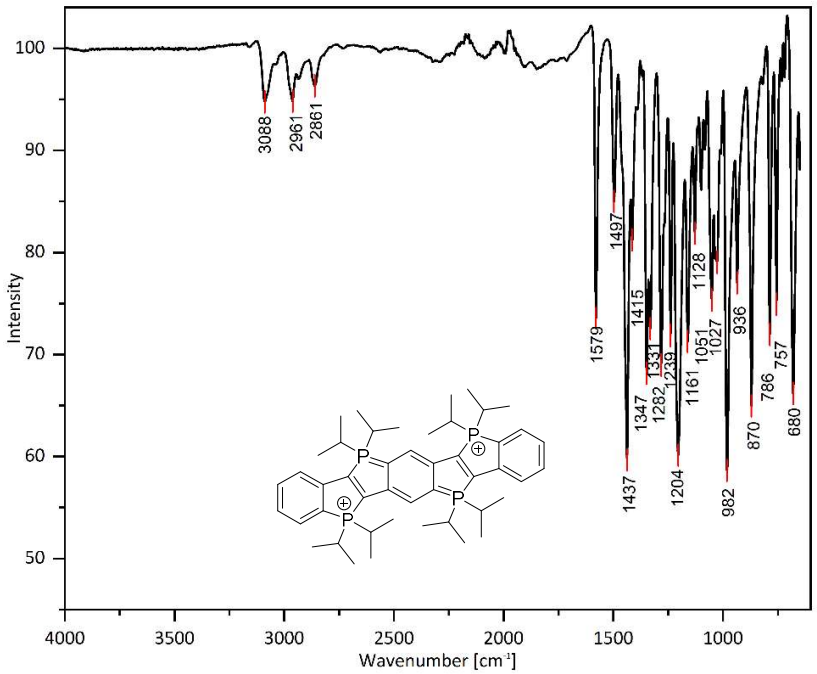

Figure 40: ATR-IR spectrum of **9** at rt under argon.

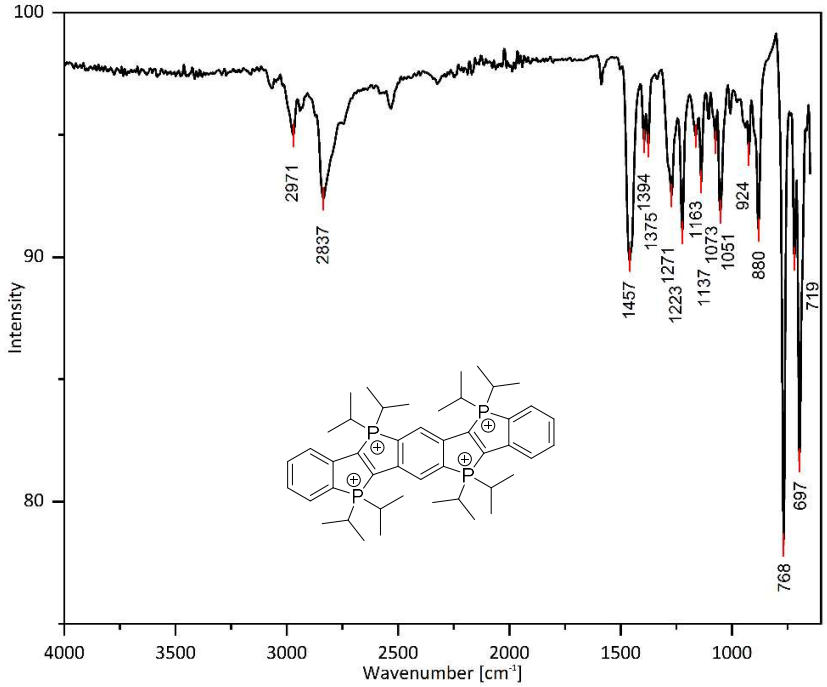

Figure 41: ATR-IR spectrum of **7** at rt under argon.

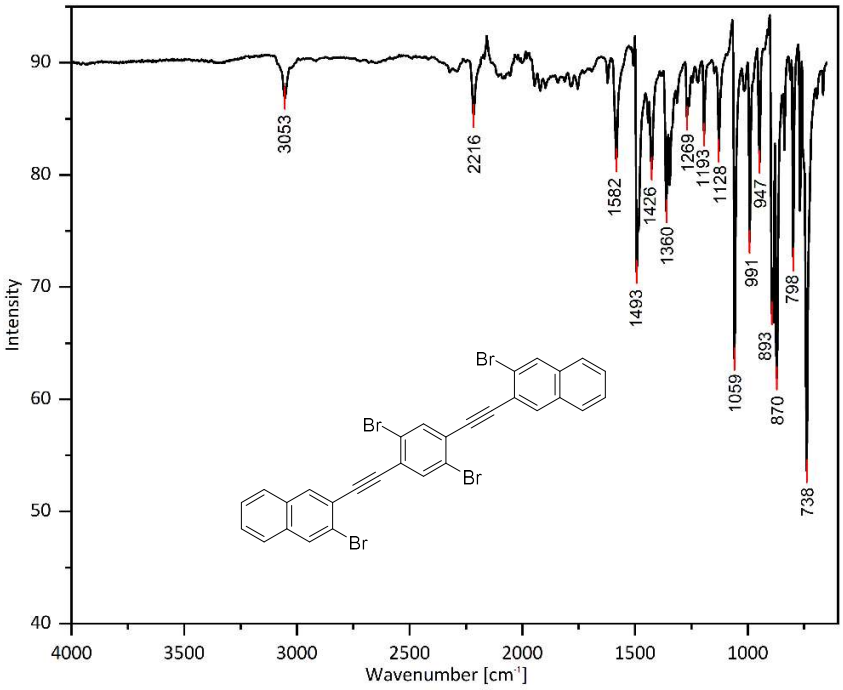

Figure 42: ATR-IR spectrum of **4** at rt under argon.

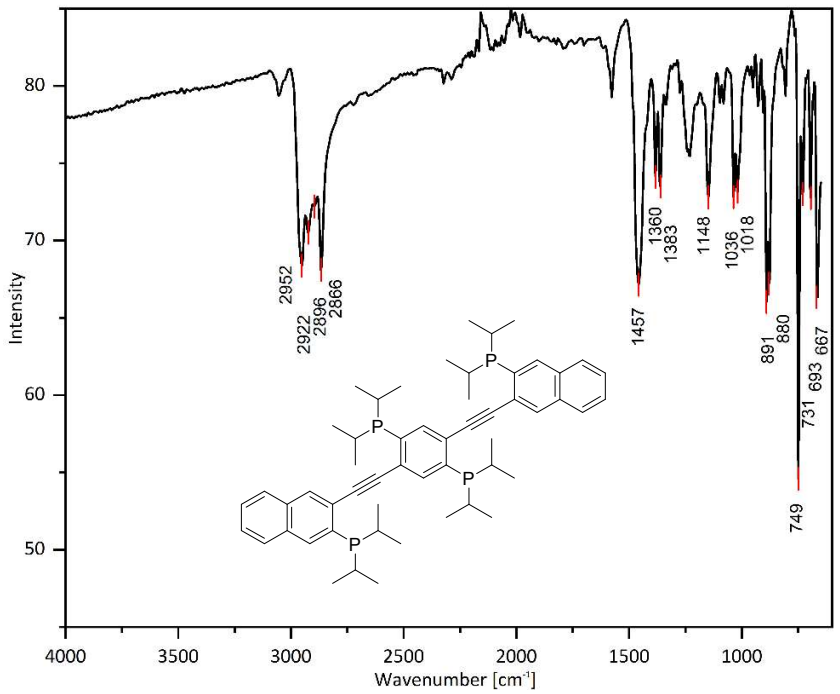

Figure 43: ATR-IR spectrum of **6** at rt under argon.

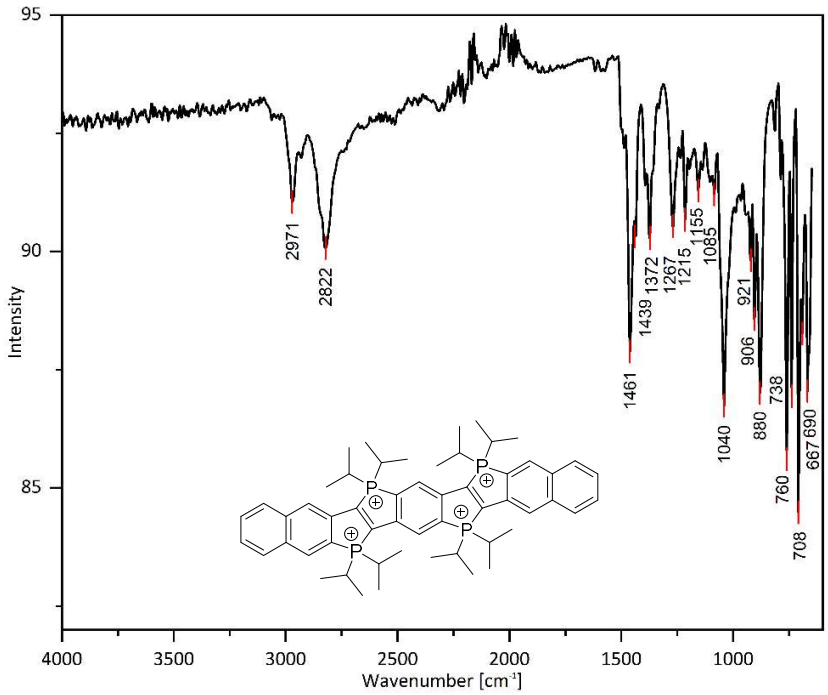

Figure 44: ATR-IR spectrum of **8** at rt under argon.

7) EPR: Computational Modeling

Computational modeling of EPR was carried out using ORCA 6.1.0.[11] All structures were optimized without symmetry restrictions, and the final geometries were confirmed as true minima by frequency analysis at the UKS r^{2}SCAN-3c/def2-mTZVPP level of theory.[12-15] To improve computational efficiency, the resolution-of-the-identity (RI) approximation was employed in combination with the def2-mTZVPP/J auxiliary basis set.[12]

In Figure 45, Figure 46 and Figure 47 the experimental spectra of [**PhPhPh**]$^{1+}$ and [**PhPhPh**]$^{3+}$ are compared with the computed spectra, which were plotted using EasySpin v6.0.9 and Matlab R2025a.[1-3] Considering the discrepancy observed in Figure 46 and the overall good agreement in Figure 45, it can be concluded that the experimental spectrum of [**PhPhPh**]$^{1+}$ is more consistent with a one-side-cyclized structure rather than a two-side-cyclized structure.

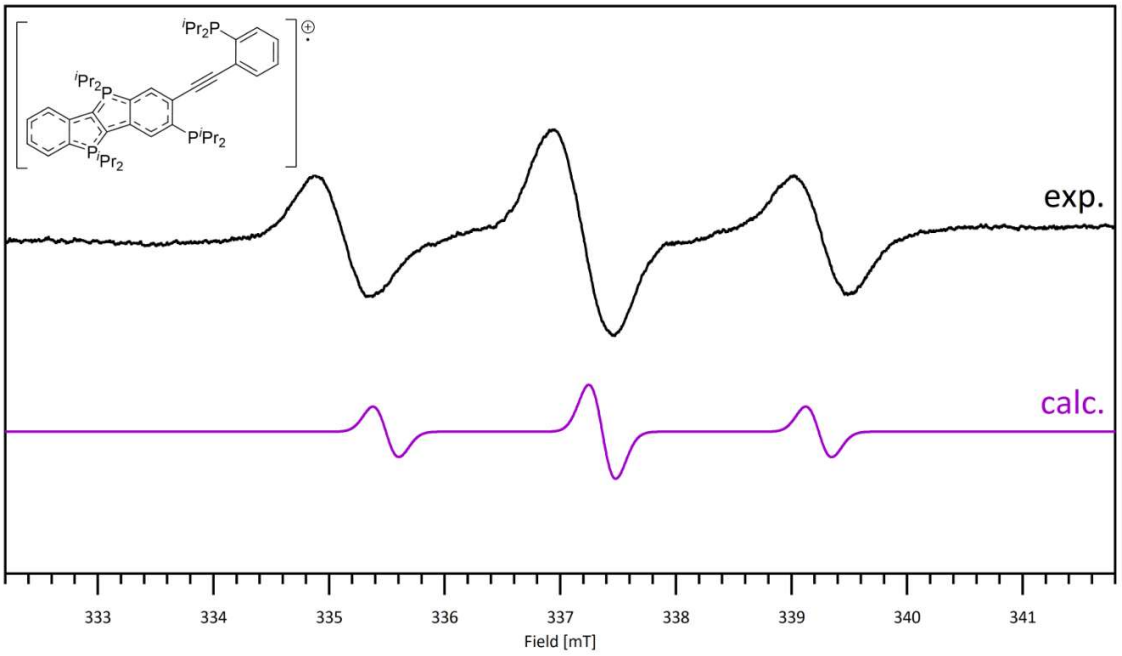

Figure 45: X-band EPR experimental data (v = 9.443296 GHz; g_{iso} = 2.0012) of [**PhPhPh**]$^{1+}$ in CH_2Cl_2 at rt (see Figure 18, fitting parameters: g_{iso} = 2.0022; $A_{iso1,sim}(^{31}P)$ = -58.2756 MHz; $A_{iso2,sim}(^{31}P)$ = -55.4521 MHz; $A_{iso3,sim}(^{31}P)$ = 4.3381 MHz; $A_{iso4,sim}(^{31}P)$ = 6.0927 MHz) compared to computed data for a one-side-cyclized structure (UKS B3LYP/def2-TZVPP, calc. values: $g_{iso,calc}$ = 2.0026; $A_{iso1,calc}(^{31}P)$ = -53.2784 MHz; $A_{iso2,calc}(^{31}P)$ = -51.5930 MHz; $A_{iso3,calc}(^{31}P)$ = -0.4774 MHz; $A_{iso4,calc}(^{31}P)$ = 1.1490 MHz).

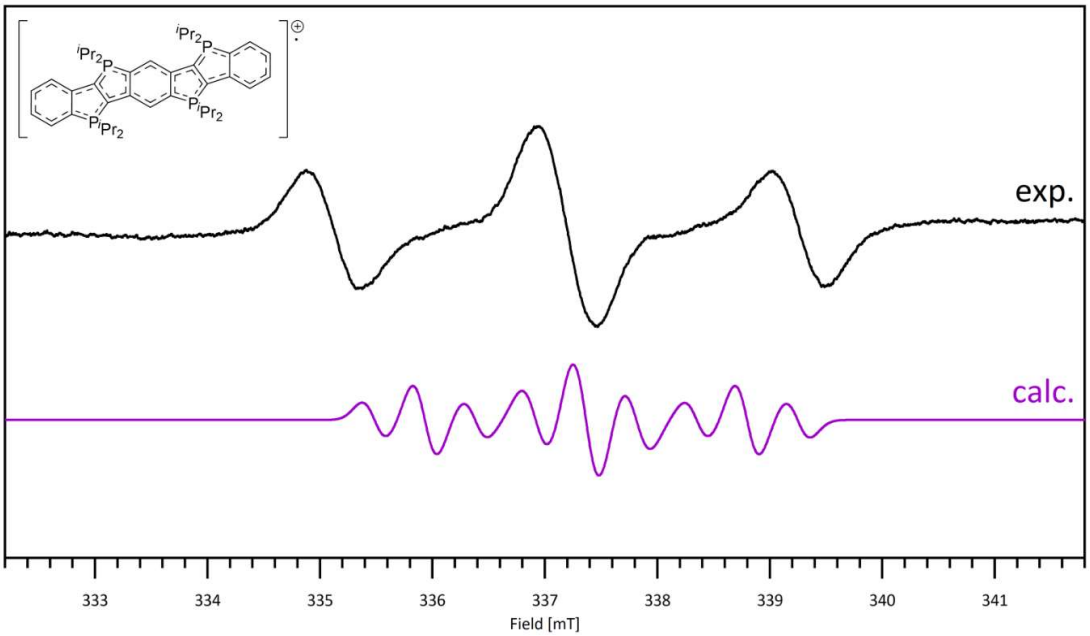

Figure 46: X-band EPR experimental data (v = 9.443296 GHz; g_{iso} = 2.0012) of [**PhPhPh**]$^{1+}$ in CH_2Cl_2 at rt (see Figure 18, fitting parameters: g_{iso} = 2.0022; $A_{iso1,sim}(^{31}P)$ = -58.2756 MHz; $A_{iso2,sim}(^{31}P)$ = -55.4521 MHz; $A_{iso3,sim}(^{31}P)$ = 4.3381 MHz; $A_{iso4,sim}(^{31}P)$ = 6.0927 MHz) compared to computed data for a two-side-cyclized structure (UKS B3LYP/def2-TZVPP, calc. values: $g_{iso,calc}$ = 2.0028; $A_{iso1,calc}(^{31}P)$ = -38.8115 MHz; $A_{iso2,calc}(^{31}P)$ = -12.5816 MHz; $A_{iso3,calc}(^{31}P)$ = -12.5526 MHz; $A_{iso4,calc}(^{31}P)$ = -41.4303 MHz). **Considering the differences between the experimental and computed spectra, it can be concluded that the measured spectrum is more consistent with a one-side-cyclized structure.**

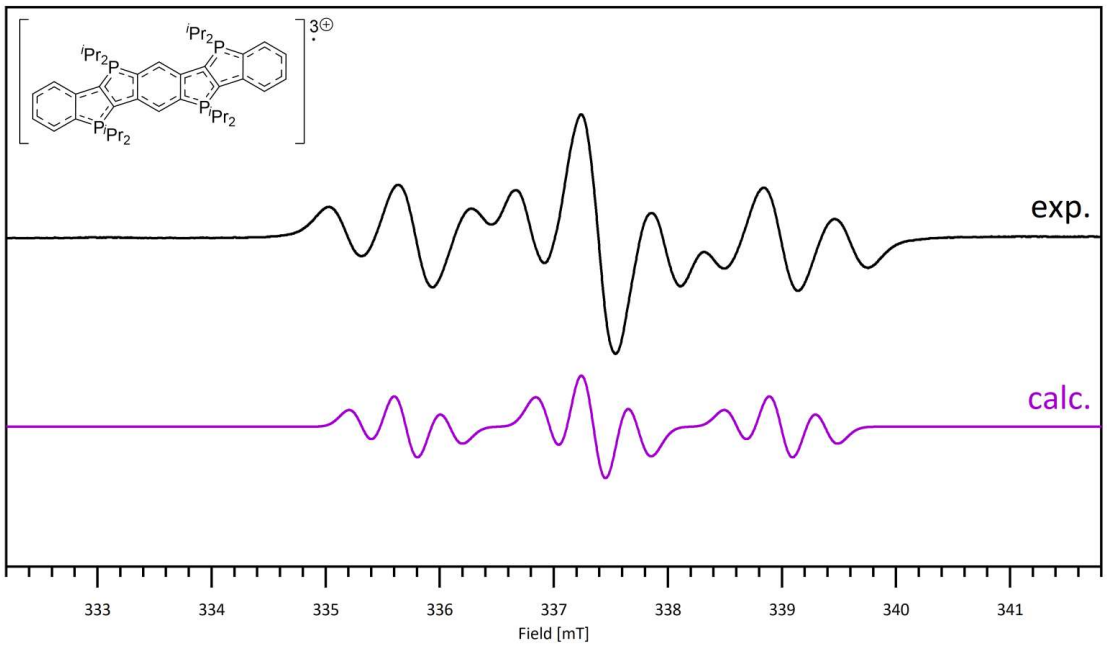

Figure 47: X-band EPR experimental data (v = 9.449465 GHz; g_{iso} = 2.0013) of [**PhPhPh**]$^{3+}$ in CH_2Cl_2 at rt (see Figure 19, fitting parameters: g_{iso} = 2.0011; $A_{iso1,sim}(^{31}P)$ = -17.6844 MHz; $A_{iso2,sim}(^{31}P)$ = -43.7523 MHz; $A_{iso3,sim}(^{31}P)$ = -46.0084 MHz; $A_{iso4,sim}(^{31}P)$ = -15.0754 MHz) compared to computed data (UKS B3LYP/def2-TZVPP, calc. values: $g_{iso,calc}$ = 2.0025; $A_{iso1,calc}(^{31}P)$ = -11.2184 MHz; $A_{iso2,calc}(^{31}P)$ = -47.1724 MHz; $A_{iso3,calc}(^{31}P)$ = -44.9409 MHz; $A_{iso4,calc}(^{31}P)$ = -10.4910 MHz).

8) ACID (Anisotropy of the Induced Current Density) Plots

NMR computations were performed in Gaussian 16 (G16 Rev. C.01)[16] using the CSGT method at the B3LYP-D3(BJ)/def2-TZVPP[17-22] level of theory with the keyword iop(10/93=1). Solvent effects were accounted for using the polarizable continuum model (PCM) with dichloromethane as the solvent (SCRF = (SMD, solvent = dichloromethane)).[23, 24] Anisotropy of the induced current density (ACID) computations were carried out with AICD-3.0.4 and visualized using POV-Ray 3.7.0.[25-27]

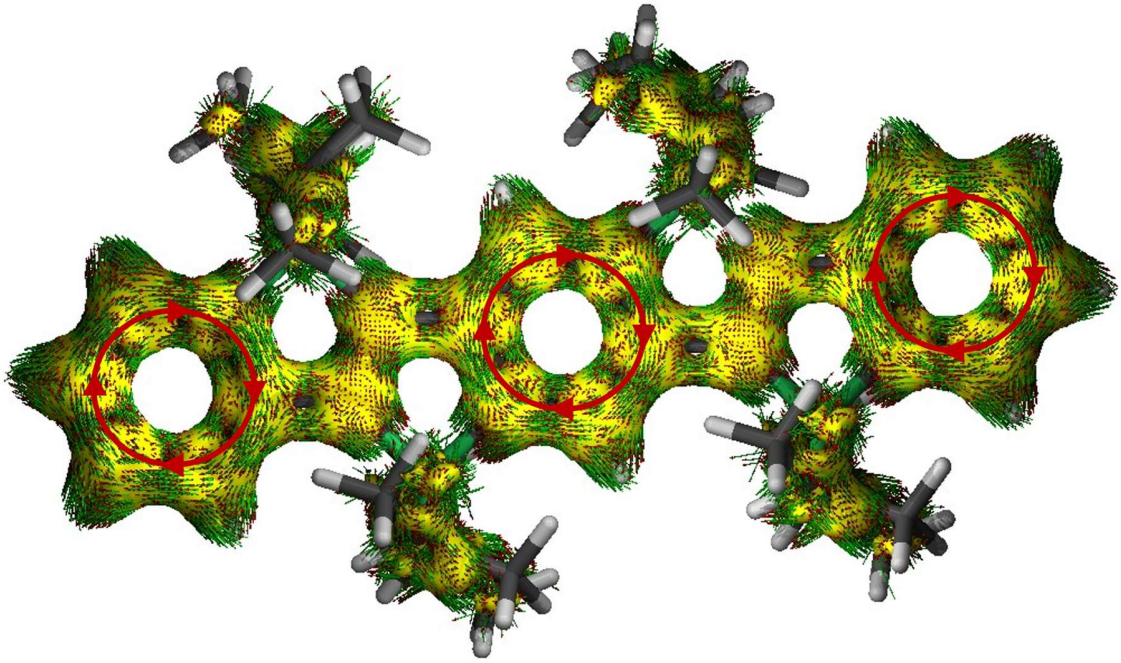

Figure 48: Anisotropy of the induced current density (ACID) plots for **7** ([**PhPhPh**]$^{4+}$) (B3LYP, def2-TZVPP, GD3BJ, SCRF for CH_2Cl_2, isovalue = 0.05 (default)). Diatropic ring currents are visualized by red circular arrows, indicating aromaticity. In contrast, the current density vectors at the C=C bond connecting the two P^+ atoms point toward the observer (out of the plane).

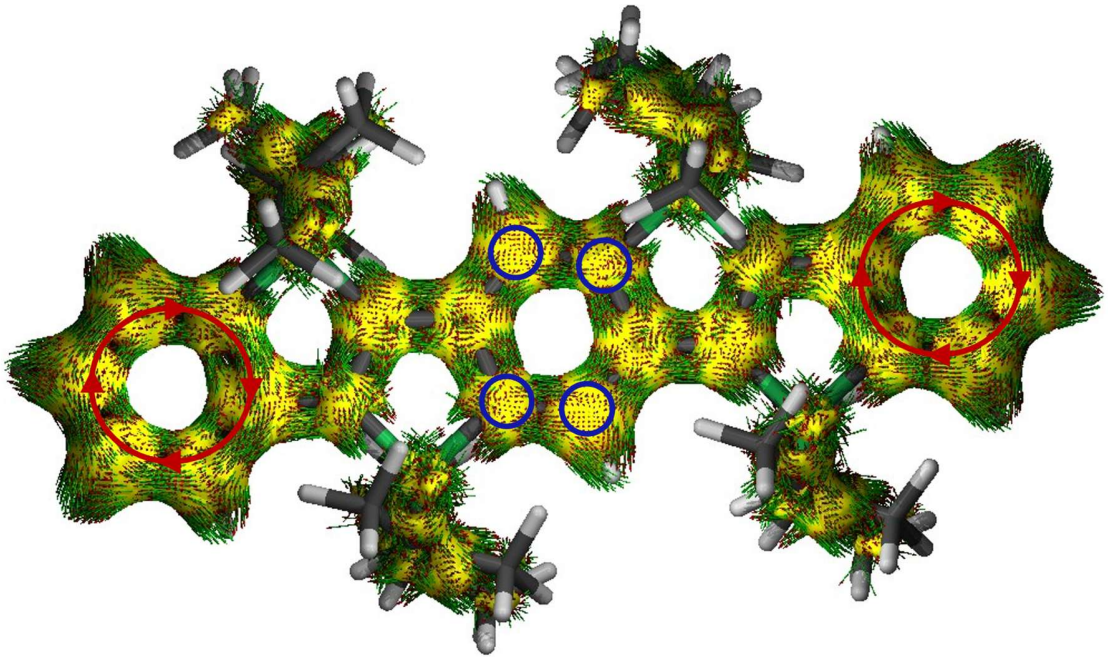

Figure 49: Anisotropy of the induced current density (ACID) plots for **9** ([**PhPhPh**]$^{2+}$) (B3LYP, def2-TZVPP, GD3BJ, SCRF for CH_2Cl_2, isovalue = 0.05 (default)). Diatropic ring currents are visualized by red circular arrows, indicating aromaticity. In contrast to **7** ([**PhPhPh**]$^{4+}$), the current density vectors of the central C_6 unit (blue circles) point toward the observer (out of the plane), indicating decreased aromaticity.

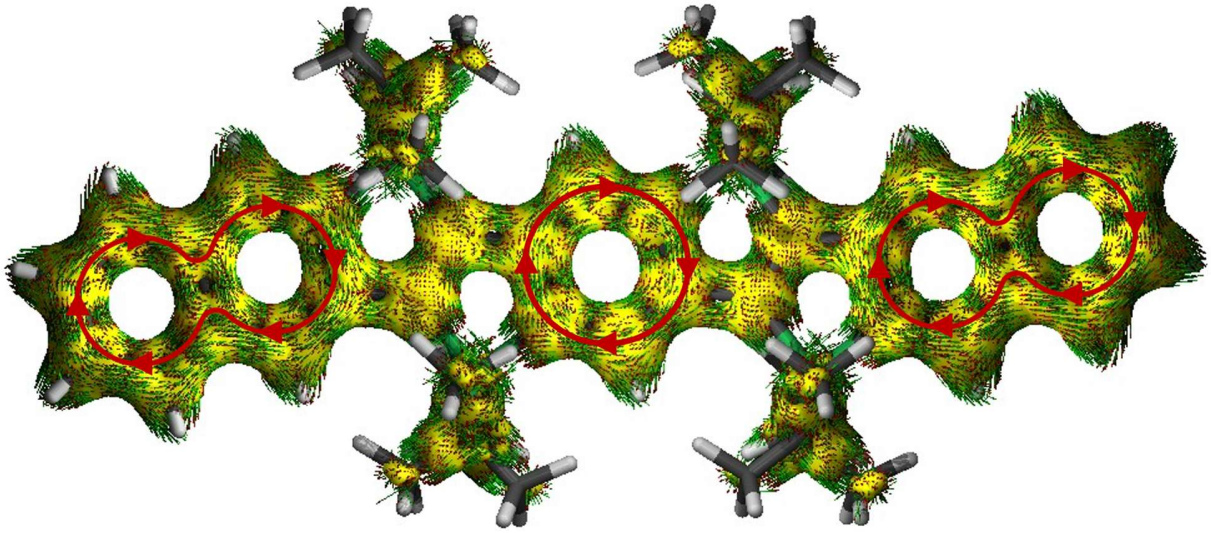

Figure 50: Anisotropy of the induced current density (ACID) plots for **8** ([**NapPhNap**]$^{4+}$) (B3LYP, def2-TZVPP, GD3BJ, SCRF for CH_2Cl_2, isovalue = 0.05 (default)). Diatropic ring currents are visualized by red circular arrows, indicating aromaticity. In contrast, the current density vectors at the C=C bond connecting the two P^+ atoms point toward the observer (out of the plane).

9) NICS (Nucleus Independent Chemical Shift) Plots

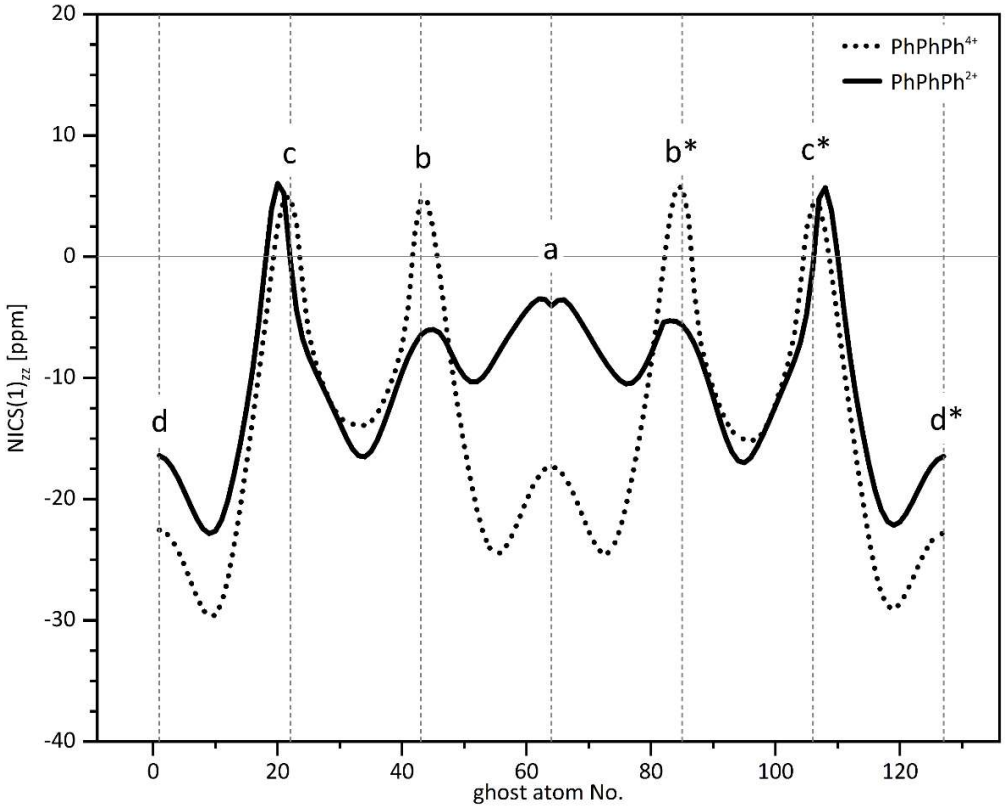

Figure 51: NICS(1)$_{zz}$-*XY* scans of **7** ([**PhPhPh**]$^{4+}$) and **9** ([**PhPhPh**]$^{2+}$) in comparison (B3LYP, def2-TZVPP, D3BJ, CPCM for CH_2Cl_2), starting in the centre of (d). This scan suggests that the five-membered ring cores (rings b, b*, c, and c*) are electronically decoupled from the peripheral arenes. The positive NICS(1)$_{zz}$ values of these five-membered rings are not indicative of antiaromaticity, as constrained trans-stilbene showed similar values in our previous study.[28] The increased NICS(1)$_{zz}$ values of **9** for ring (a) indicate a decrease in aromaticity, whereas the decreased NICS(1)$_{zz}$ values of rings (b) and (b*) for the same compound suggest enhanced electronic delocalization compared to **7**.

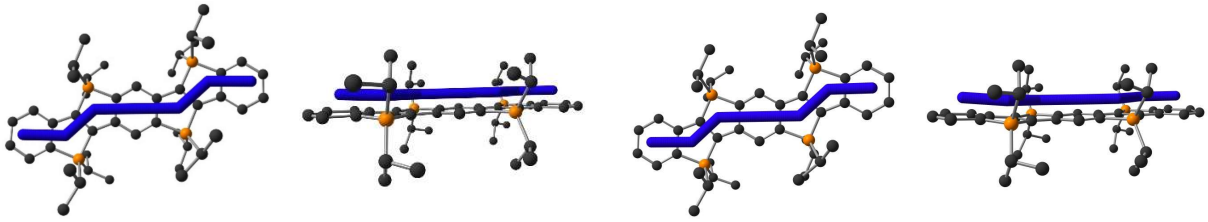

Figure 52: NICS(1)$_{zz}$-*XY* scan trajectories of the ghost atoms for **7** ([**PhPhPh**]$^{4+}$, left) and **9** ([**PhPhPh**]$^{2+}$, right). One ghost atom was placed 1 Å above the mean plane of each ring center. Between these initially placed ghost atoms, 20 additional ghost atoms were distributed equidistantly along a straight line.

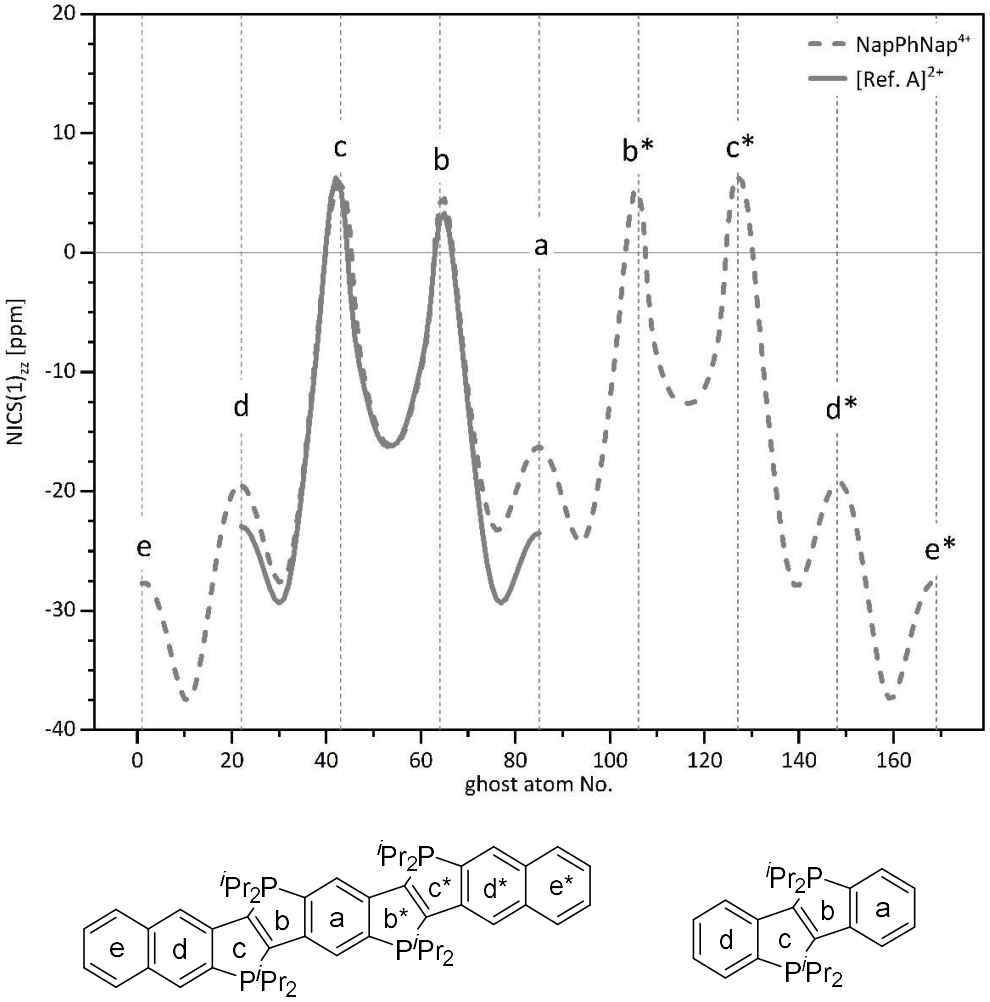

Figure 53: NICS(1)$_{zz}$-*XY* scans of **8** ([**NapPhNap**]$^{4+}$) and [**ref. A**][29] ([**PhPh**]$^{2+}$) in comparison (B3LYP, def2-TZVPP, D3BJ, CPCM for CH_2Cl_2), starting in the centre of (e). This scan suggests that the five-membered ring cores (rings b, b*, c, and c*) are electronically decoupled from the peripheral arenes. The positive NICS(1)$_{zz}$ values of these five-membered rings are not indicative of antiaromaticity, as constrained trans-stilbene and [**ref. A**] showed similar values in our previous study.[28]

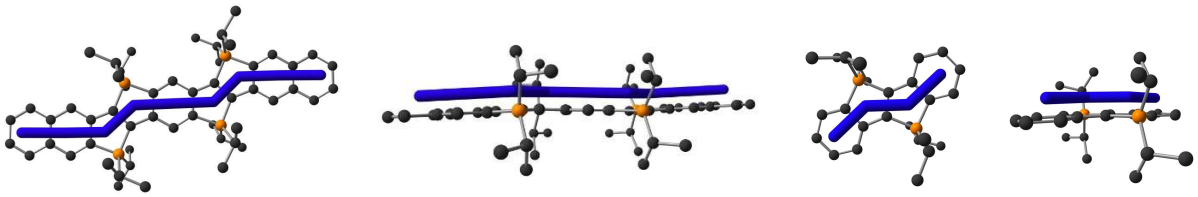

Figure 54: NICS(1)$_{zz}$-*XY* scan trajectories of the ghost atoms for **8** ([**NapPhNap**]$^{4+}$, left) and [**ref. A**] ([**PhPh**]$^{2+}$, right). One ghost atom was placed 1 Å above the mean plane of each ring center. Between these initially placed ghost atoms, 20 additional ghost atoms were distributed equidistantly along a straight line.

10) Single Crystal X-Ray Structure Analysis

Crystal data and details of the structure determinations are compiled in Table 3. Full shells of intensity data were collected at 120(1) K with an Agilent Technologies Supernova-E CCD diffractometer (Cu-K_α radiation, microfocus X-ray tube, multilayer mirror optics). Detector frames (typically ω-, occasionally φ-scans, scan width 1.0°) were integrated by profile fitting.[30, 31] Data were corrected for air and detector absorption, Lorentz and polarization effects[32-34] and scaled essentially by application of appropriate spherical harmonic functions.[35-37] Absorption by the crystal was treated numerically (Gaussian grid).[37, 38] An illumination correction was performed as part of the numerical absorption correction.[37]

Using OLEX2,[39] the structures were solved with SHELXT[40, 41] (intrinsic phasing) and refined with SHELXL[42-44] by full-matrix least squares methods based on F^2 against all unique reflections. All non-hydrogen atoms were given anisotropic displacement parameters. Hydrogen atoms were generally input at calculated positions and refined with a riding model.[45-49] Split atom models were used to refine disordered groups and/or solvent molecules. When found necessary, suitable geometry and adp restraints were applied.[45-49]

In structure CCDC 2525134, disordered Et_2O solvent molecules (one molecule per formula unit) were treated with OLEX2 solvent masks. In structure CCDC 2525135, disordered water molecules (four molecules per asymmetric unit, corresponding to eight molecules per formula unit) were treated with OLEX2 solvent masks. In structure CCDC 2525136, disordered MeOH solvent molecules (one molecule per asymmetric unit, corresponding to two molecules per formula unit) were treated with OLEX2 solvent masks.

CCDC 2525134 – 2525136 contain the supplementary crystallographic data for this paper. These data can be obtained free of charge from the Cambridge Crystallographic Data Centre's and FIZ Karlsruhe's joint Access Service via https://www.ccdc.cam.ac.uk.

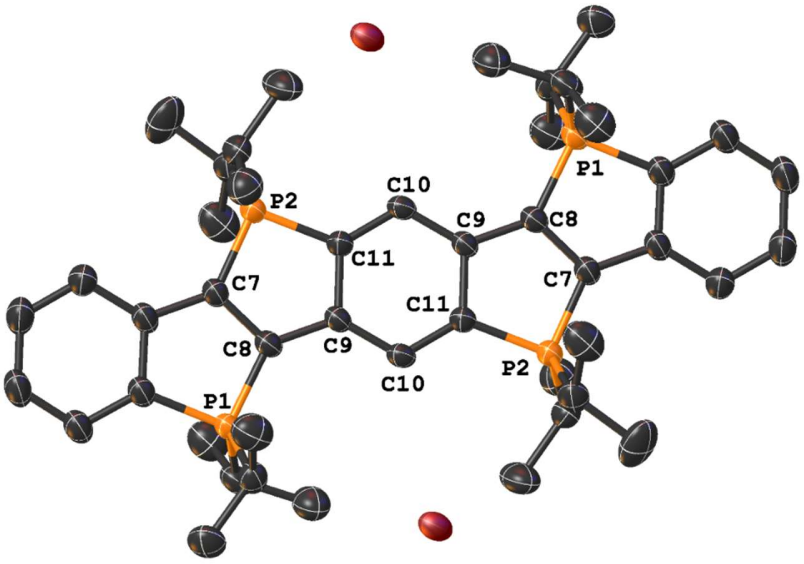

Figure 55: ORTEP-plot of the molecular structure of **9** ([**PhPhPh**]Br_2) (thermal ellipsoids at 50% probability; hydrogen atoms and disordered diethyl ether molecules omitted for clarity). Selected bond lengths (Å) and angles (°): P1–C8 1.776(2), C7–C8 1.417(3), P2–C7 1.758(2), P2–C11^1 1.793(2), C9–C10 1.401(3), C10–C11 1.381(3), C11–C9^1 1.452(3), P1–C8–C9 135.65(19), P1–C8–C7 107.77(17), P2–C7–C8 109.06(17), C7–C8–C9 116.5(2).

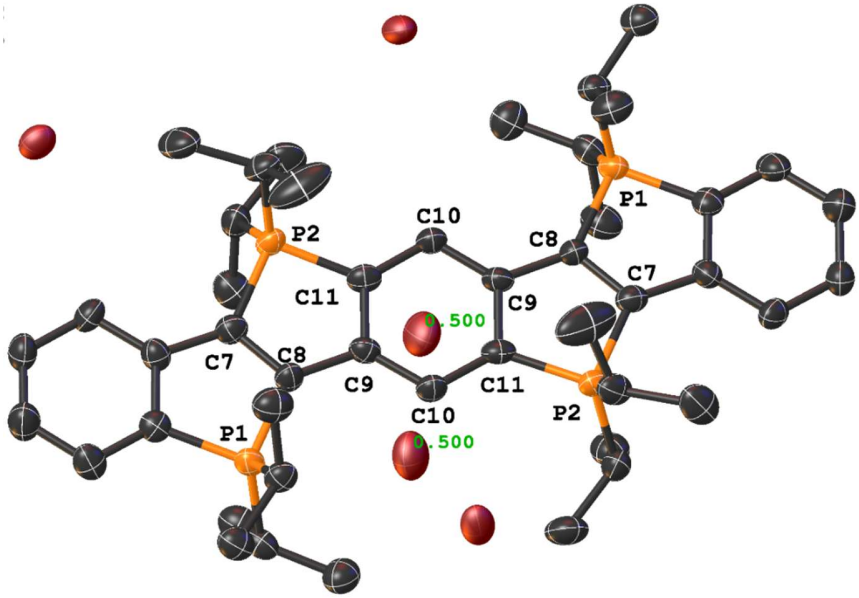

Figure 56: ORTEP-plot of the molecular structure of **7** ([**PhPhPh**]Br_4) (thermal ellipsoids at 50% probability; hydrogen atoms and disordered water molecules omitted for clarity; chrystallographic occupancy of two bromine atoms is 0.5). Selected bond lengths (Å) and angles (°): P1–C8 1.807(6), C7–C8 1.359(9), P2–C7 1.817(7), P2–C11^1 1.792(7), C9–C10 1.387(9), C10–C11 1.418(10), C11–C9^1 1.389(8), P1– C8–C9 135.7(4), P1–C8–C7 107.3(5), P2–C7–C8 107.9(5), C7–C8–C9 116.9(5).

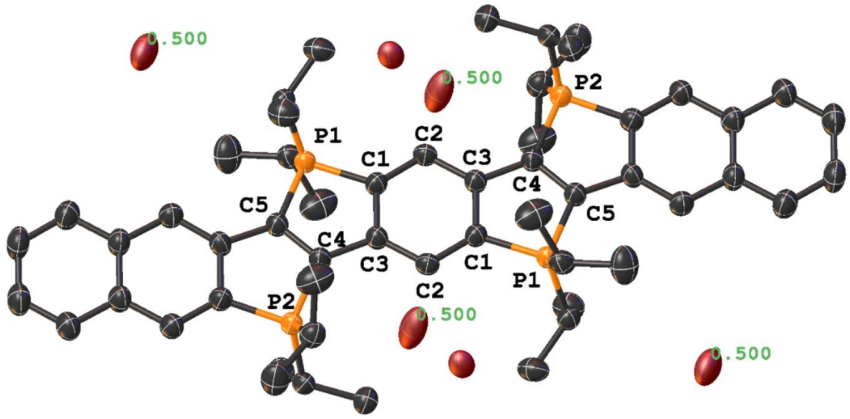

Figure 57: ORTEP-plot of the molecular structure of **8** ([**NapPhNap**]Br_4) (thermal ellipsoids at 50% probability; hydrogen atoms omitted for clarity; occupancy of four bromine atoms is 0.5). Selected bond lengths (Å) and angles (°): P2–C4 1.809(3), C4–C5 1.357(4), P1–$C5^1$ 1.800(3), C3–C2 1.393(5), C2–C1 1.385(5), C1–$C3^1$ 1.414(5), P2–C4–C3 134.3(2), P2–C4–C5 109.0(2), $P1^1$–C5–C4 109.1(2), C5–C4–C3 116.8(3).

Table 3: Crystal data and details of the structure determinations for [**PhPhPh**]Br_2 × Et_2O, [**PhPhPh**]Br_4 × 8 H_2O and [**NapPhNap**]Br_4 × 2 MeOH.

Compound	(**9**) [**PhPhPh**]Br_2 × Et_2O	(**7**) [**PhPhPh**]Br_4 × 8 H_2O	(**8**) [**NapPhNap**]Br_4 × 2 MeOH
Empirical formula	$C_{50}H_{76}Br_2OP_4$	$C_{46}H_{82}Br_4O_8P_4$	$C_{56}H_{78}Br_4O_2P_4$
Formula weight	976.80	1206.63	1226.70
Temperature [K]	120(1)	120(1)	120(1)
Crystal system	*monoclinic*	*trigonal*	*monoclinic*
Space group (number)	*$P2_1/c$* (14)	*$P3_221$* (154)	*C2/c* (15)
a [Å]	12.5338(2)	12.4139(3)	23.0439(3)
b [Å]	15.7508(2)	12.4139(3)	8.59720(10)
c [Å]	14.4968(3)	32.4727(5)	30.0718(4)
α [°]	90	90	90
β [°]	115.625(2)	90	102.5950(10)
γ [°]	90	120	90
Volume [$Å^3$]	2580.43(8)	4333.8(2)	5814.25(13)
Z	2	3	4
ρ_{calc} [gcm^{-3}]	1.257	1.387	1.401
μ [mm^{-1}]	3.408	4.800	4.707
F(000)	1028.0	1866	2520.0
Radiation	Cu-K_α (λ = 1.54184)	Cu-K_α (λ = 1.54184 Å)	Cu-K_α (λ = 1.54184)
2θ range [°]	7.824 to 142.192 (0.81 Å)	8.168 to 142.398 (0.81 Å)	6.022 to 141.94 (0.82 Å)
Index ranges	-15 ≤ h ≤ 15 -19 ≤ k ≤ 19 -17 ≤ l ≤ 14	-14 ≤ h ≤ 14 -14 ≤ k ≤ 13 -34 ≤ l ≤ 39	-27 ≤ h ≤ 28 -10 ≤ k ≤ 10 -36 ≤ l ≤ 36
Reflections collected	38166	33705	38736
Independent reflections	4956 (R_{int} = 0.0454)	5564 (R_{int} = 0.0811)	5572 (R_{int} = 0.0680)
Completeness to θ	99.0% (θ = 71.10°)	99.9% (θ = 71.20°)	99.2% (θ = 70.97°)
Data / Restraints / Parameters	4956/0/243	5564/0/257	5572/0/290
T_{min}/T_{max}	0.625 / 1.000	0.728 / 0.986	0.598 / 1.000
Goodness-of-fit on F^2	1.037	1.030	1.072
Final *R* indexes [$I \geq 2\sigma(I)$]	R_1 = 0.0416 wR_2 = 0.1123	R_1 = 0.0499 wR_2 = 0.1299	R_1 = 0.0531 wR_2 = 0.1541
Final *R* indexes [all data]	R_1 = 0.0451 wR_2 = 0.1157	R_1 = 0.0585 wR_2 = 0.1368	R_1 = 0.0571 wR_2 = 0.1592
Largest peak/hole [$eÅ^{-3}$]	0.93/-0.45	1.36/-0.65	1.12/-1.31
CCDC number	2525134	2525135	2525136

11) Interaction with ctDNA

The interaction of the compounds with ctDNA (Sigma Aldrich, deoxyribonucleic acid sodium salt from calf thymus, D3664) was probed using linear dichroism (LD) spectroscopy. LD spectra were recorded on a Jasco J-815 spectropolarimeter with an LD accessory using a Couette flow cell (80 µL) at a rotational speed of 3000 rpm (scanning speed 500 nm min^{-1}, 5 accumulations, 1 mM DNA (in bases, ε_{260} = 6600 L mol^{-1} cm^{-1}), ambient temperature). Buffer solution (50 mM Tris (pH 7.4), 1 mM NaCl) was prepared in deionized water. The pH was adjusted by means of an aqueous HCl solution. Samples were prepared by combining a 1 mM ctDNA solution with appropriate amounts of a 1 mM stock solution of the compound under investigation. Spectra were recorded within 5 min of sample preparation. A negative LD signal at the wavelength of absorbance of the compound under consideration indicates an intercalation into the DNA.[50]

To evaluate the solution stability of the compounds, UV/Vis absorbance spectra were recorded on a Jasco V-750 spectrometer at 20 °C in a 1 cm quartz cuvette with a scan rate of 400 nm min^{-1}, a data interval of 1.0 nm and a concentration of 10 µM. Time-dependent UV/Vis spectra were recorded analogously with a data interval of 0.5 nm at an interval of 2 min (scan time 1.92 min, waiting time 0.08 min).

The spectra shown in Figures 58 – 62 indicate that the tetracationic compounds are not suitable as DNA intercalators because either they do not intercalate (compound **7**) or they decompose rapidly in aqueous buffer solution (compound **8**).

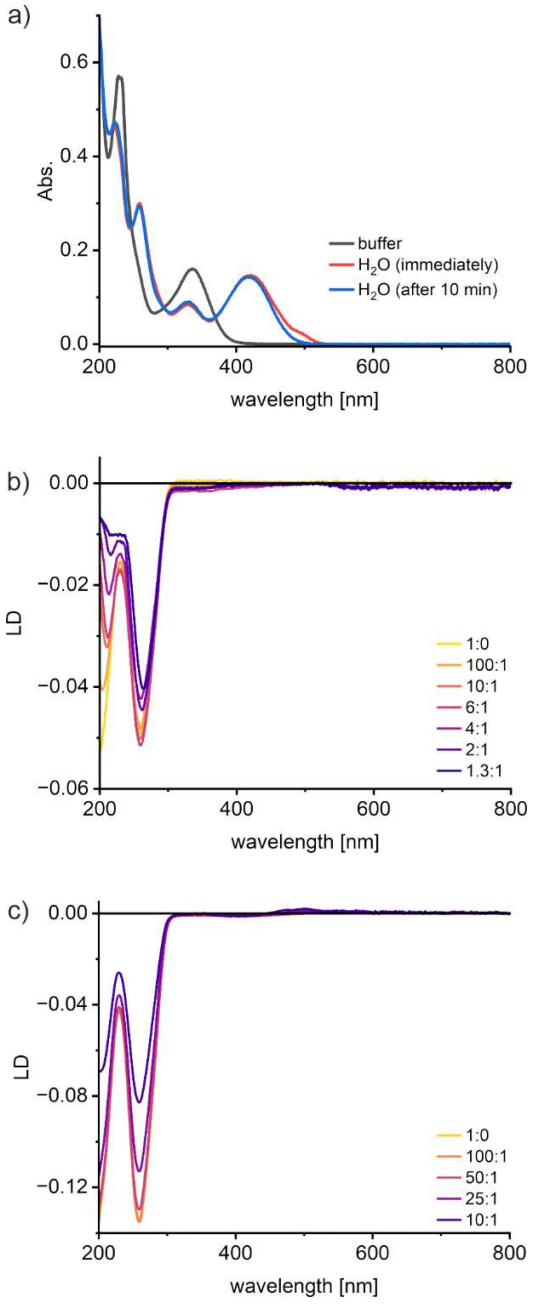

Figure 58: Investigation of compound **7** with respect to its interaction with ctDNA. a) Absorbance spectra indicate an immediate decomposition of compound **7** in buffer, whereas it is somewhat more stable in water. The LD spectra recorded in b) buffer solution and c) water do not show any indication of an intercalation into ctDNA. The decreasing intensity of the LD band of ctDNA in water at ca. 260 nm with increasing amounts of compound **7** may indicate a coiling of the DNA induced by the tetracationic compound. Experimental conditions: buffer solution = 50 mM Tris (pH 7.4), 1 mM NaCl; absorbance spectra: 10 µM compound **7**; LD spectra: 1 mM ctDNA with increasing amounts of compound **7** (ratio relative to number of DNA bases).

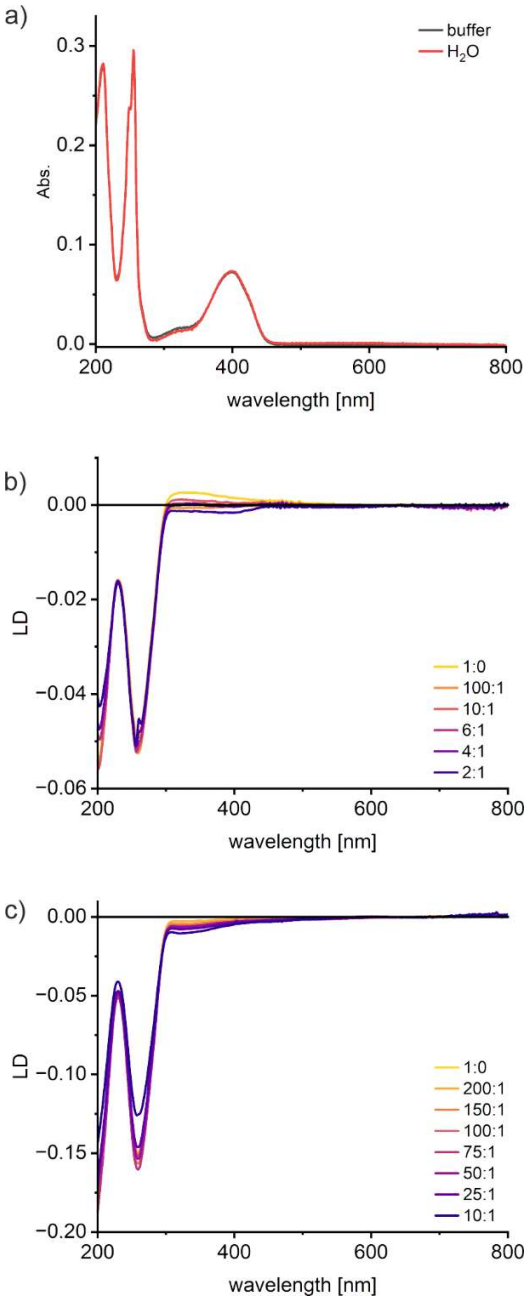

Figure 59: Investigation of the dicationic reference compound[29] [**ref. A**]Cl_2 with respect to its interaction with ctDNA. a) The perfectly overlapping absorbance spectra in buffer and water indicate good solution stability. The lack of an intense signal at ca. 400 nm in the LD spectra recorded in b) buffer solution and c) water indicates the absence of a strong interaction with ctDNA. In combination with the data obtained for compound **7** it can be concluded that the π systems of these compounds are too small for an effective intercalation. Experimental conditions: buffer solution = 50 mM Tris (pH 7.4), 1 mM NaCl; absorbance spectra: 10 µM compound [**ref. A**]Cl_2; LD spectra: 1 mM ctDNA with increasing amounts of compound [**ref. A**]Cl_2 (ratio relative to number of DNA bases).

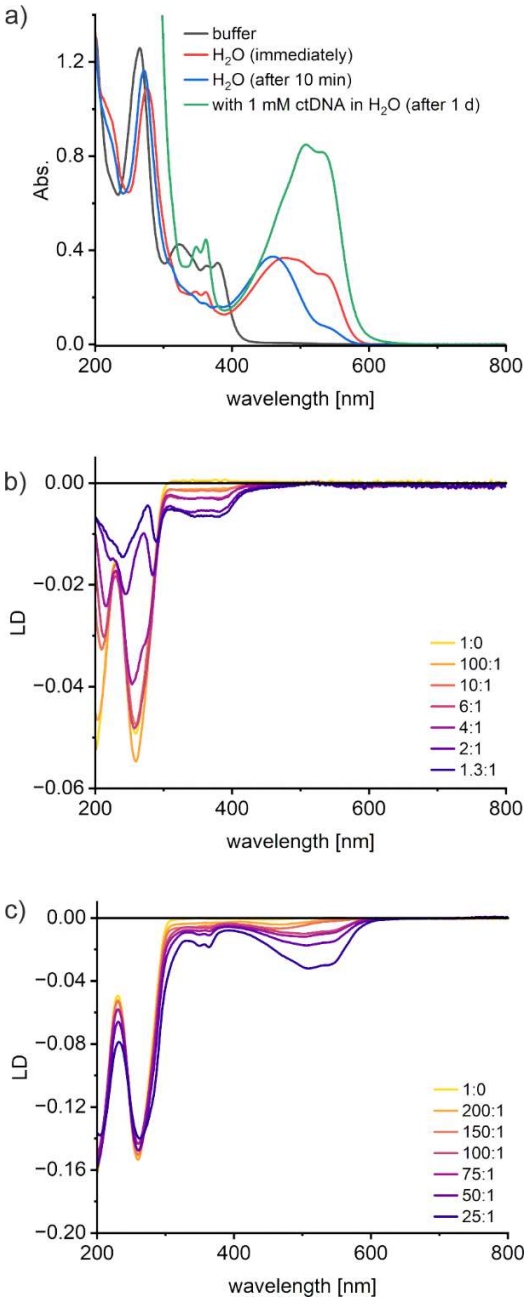

Figure 60: Investigation of compound **8** with respect to its interaction with ctDNA. a) Absorbance spectra indicate an immediate decomposition of compound **8** in buffer and a rapid decomposition in water (see also Figure 62). Once intercalated into ctDNA, compound **8** remains stable. The LD spectra recorded in b) buffer solution and c) water indicate an intercalation of the decomposition product and compound **8**, respectively, into ctDNA. The decreasing intensity of the LD band of ctDNA in buffer at ca. 260 nm with increasing amounts of the decomposition product of compound **8** may indicate a coiling of the DNA. Experimental conditions: buffer solution = 50 mM Tris (pH 7.4), 1 mM NaCl; absorbance spectra: 10 µM compound **8**; LD spectra: 1 mM ctDNA with increasing amounts of compound **8** (ratio relative to number of DNA bases).

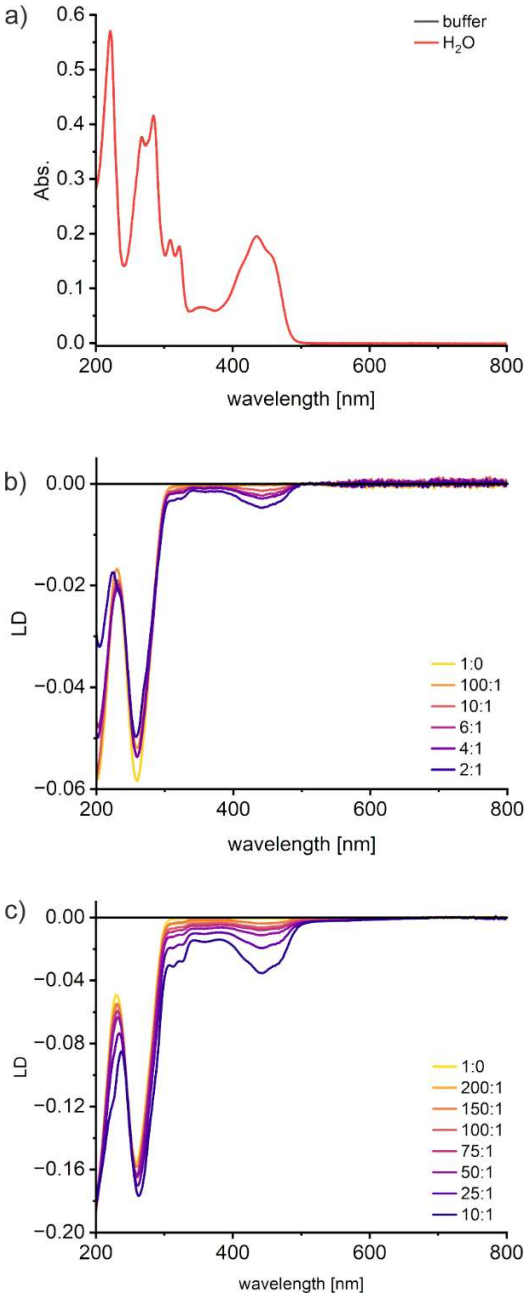

Figure 61: Investigation of the dicationic reference compound[28] [**ref. B**]Cl_2 with respect to its interaction with ctDNA. a) The perfectly overlapping absorbance spectra in buffer and water indicate good solution stability. The LD spectra recorded in b) buffer solution and c) water indicate an intercalation into ctDNA. Hence, the dicationic compound [**ref. B**]Cl_2 is better suited as a DNA intercalator than the tetracationic compound **8** because of its superior stability in aqueous solution. Experimental conditions: buffer solution = 50 mM Tris (pH 7.4), 1 mM NaCl; absorbance spectra: 10 µM compound [**ref. B**]Cl_2; LD spectra: 1 mM ctDNA with increasing amounts of compound [**ref. B**]Cl_2 (ratio relative to number of DNA bases).

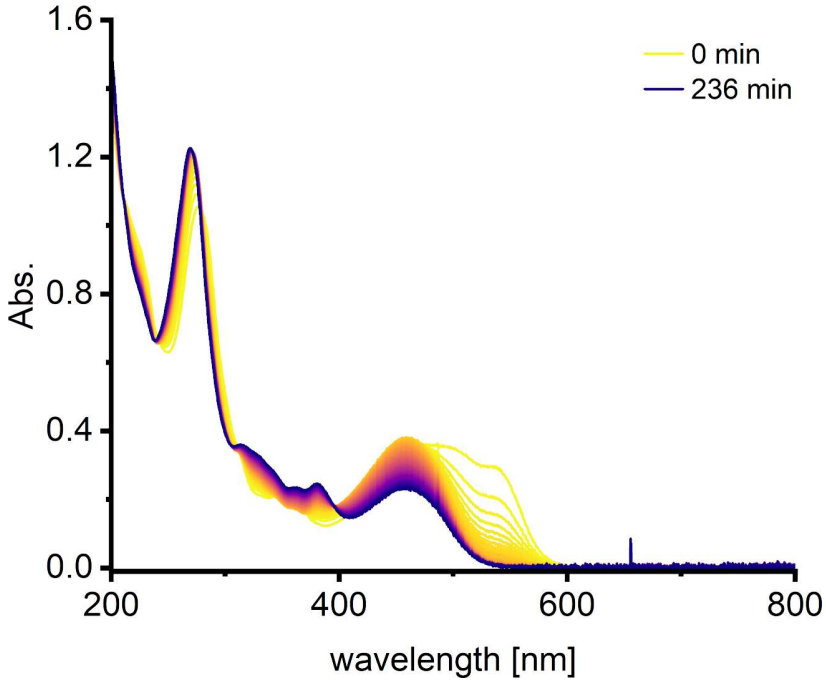

Figure 62: Time-dependent UV/Vis spectra of compound **8** in water, indicating its rapid decomposition. Experimental conditions: 10 µM compound **8** in water, spectra recorded every 2 min.

References

1. S. Stoll and A. Schweiger, *J. Magn. Reson.*, 2006, **178**, 42-55.
2. The MathWorks Inc., *MATLAB R2025a*, 2025.
3. EasySpin v6.0.9, *An open-source MATLAB toolbox for simulating and fitting a wide range of Electron Paramagnetic Resonance (EPR) spectra*, 2025.
4. K. Fuji, K. Kawashima, T. Mori, K. Sekine and Y. Kuninobu, *Org. Lett.*, 2025, **27**, 1614-1619.
5. K. Yoshida, T. Furuyama, C. Wang, A. Muranaka, D. Hashizume, S. Yasuike and M. Uchiyama, *J. Org. Chem.*, 2012, **77**, 729-732.
6. S. Yamaguchi, C. Xu and K. Tamao, *J. Am. Chem. Soc.*, 2003, **125**, 13662-13663.
7. K. Niimi, H. Mori, E. Miyazaki, I. Osaka, H. Kakizoe, K. Takimiya and C. Adachi, *Chem. Commun.*, 2012, **48**, 5892-5894.
8. M. Uryu, T. Hiraga, Y. Koga, Y. Saito, K. Murakami and K. Itami, *Angew. Chem. Int. Ed.*, 2020, **59**, 6551-6554.
9. R. E. Messersmith, M. A. Siegler and J. D. Tovar, *Synlett*, 2018, **29**, 2499-2502.
10. S. Yamaguchi, M. Taki, Tokai National Higher Education and Research System, patent JP2023130947A, 2023.
11. F. Neese, F. Wennmohs, U. Becker and C. Riplinger, *J. Chem. Phys.*, 2020, **152**, 224108.
12. S. Grimme, A. Hansen, S. Ehlert and J.-M. Mewes, *J. Chem. Phys.*, 2021, **154**, 064103.
13. J. W. Furness, A. D. Kaplan, J. Ning, J. P. Perdew and J. Sun, *J. Phys. Chem. Lett.*, 2020, **11**, 8208-8215.
14. H. Kruse and S. Grimme, *J. Chem. Phys.*, 2012, **136**, 154101.
15. S. Ehlert, U. Huniar, J. Ning, J. W. Furness, J. Sun, A. D. Kaplan, J. P. Perdew and J. G. Brandenburg, *J. Chem. Phys.*, 2021, **154**, 061101.
16. M. J. Frisch, G. W. Trucks, H. B. Schlegel, G. E. Scuseria, M. A. Robb, J. R. Cheeseman, G. Scalmani, V. Barone, G. A. Petersson, H. Nakatsuji, X. Li, M. Caricato, A. V. Marenich, J. Bloino, B. G. Janesko, R. Gomperts, B. Mennucci, H. P. Hratchian, J. V. Ortiz, A. F. Izmaylov, J. L. Sonnenberg, D. Williams-Young, F. Ding, F. Lipparini, F. Egidi, J. Goings, B. Peng, A. Petrone, T. Henderson, D. Ranasinghe, V. G. Zakrzewski, J. Gao, N. Rega, G. Zheng, W. Liang, M. Hada, M. Ehara, K. Toyota, R. Fukuda, J. Hasegawa, M. Ishida, T. Nakajima, Y. Honda, O. Kitao, H. Nakai, T. Vreven, K. Throssell, J. A. Montgomery Jr., J. E. Peralta, F. Ogliaro, M. J. Bearpark, J. J. Heyd, E. N. Brothers, K. N. Kudin, V. N. Staroverov, T. A. Keith, R. Kobayashi, J. Normand, K. Raghavachari, A. P. Rendell, J. C. Burant, S. S. Iyengar, J. Tomasi, M. Cossi, J. M. Millam, M. Klene, C. Adamo, R. Cammi, J. W. Ochterski, R. L. Martin, K. Morokuma, O. Farkas, J. B. Foresman and D. J. Fox, *Gaussian 16 Rev. C.01*, Wallingford CT, 2019.
17. A. D. Becke, *J. Chem. Phys.*, 1993, **98**, 5648-5652.
18. C. Lee, W. Yang and R. G. Parr, *Phys. Rev. B*, 1988, **37**, 785-789.
19. P. J. Stephens, F. J. Devlin, C. F. Chabalowski and M. J. Frisch, *J. Phys. Chem.*, 1994, **98**, 11623-11627.
20. F. Weigend and R. Ahlrichs, *Phys. Chem. Chem. Phys.*, 2005, **7**, 3297-3305.

21. S. Grimme, S. Ehrlich and L. Goerigk, *J. Comput. Chem.*, 2011, **32**, 1456-1465.
22. S. Grimme, J. Antony, S. Ehrlich and H. Krieg, *J. Chem. Phys.*, 2010, **132**, 154104.
23. J. Tomasi, B. Mennucci and R. Cammi, *Chem. Rev.*, 2005, **105**, 2999-3094.
24. A. V. Marenich, C. J. Cramer and D. G. Truhlar, *J. Phys. Chem. B*, 2009, **113**, 6378-6396.
25. D. Geuenich, K. Hess, F. Köhler and R. Herges, *Chem. Rev.*, 2005, **105**, 3758-3772.
26. R. Herges and D. Geuenich, *J. Phys. Chem. A*, 2001, **105**, 3214-3220.
27. Persistence of Vision Pty. Ltd., *POV-Ray Version 3.7*, Williamstown, Victoria, Australia, 2019, https://www.povray.org.
28. S. Senn, J.-M. Mörsdorf, M.-S. Bertrams, C. Kerzig and J. Ballmann, *Chem. Sci.*, 2025, **16**, 20517-20526.
29. P. Federmann, H. K. Wagner, P. W. Antoni, J.-M. Mörsdorf, J. L. Pérez Lustres, H. Wadepohl, M. Motzkus and J. Ballmann, *Org. Lett.*, 2019, **21**, 2033-2038.
30. W. Kabsch, in *International Tables for Crystallography, Vol. F: Crystallography of Biological Macromolecules*, eds. M. G. Rossmann and E. Arnold, Springer, Dordrecht, 2001, pp. 218–225.
31. Agilent Technologies UK Ltd., *CrysAlisPro*, Agilent Technologies UK Ltd., Oxford, UK, 2011-2014.
32. Bruker AXS GmbH, *SAINT*, Karlsruhe, Germany, 1997-2013.
33. Bruker AXS Inc., *SAINT V8.40A*, Madison, WI, USA, 2018.
34. Rigaku Oxford Diffraction, *CrysAlisPro*, Wrocław, Poland, 2015–2024.
35. R. H. Blessing, *Acta Crystallogr.*, 1995, **A51**, 33–38.
36. G. M. Sheldrick, *SADABS*, Bruker AXS GmbH, Karlsruhe, Germany, 2004–2014.
37. Rigaku Oxford Diffraction, *SCALE3 ABSPACK (CrysAlisPro)*, Wrocław, Poland, 2015–2024.
38. W. R. Busing and H. A. Levy, *Acta Crystallogr.*, 1957, **10**, 180-182.
39. O. V. Dolomanov, L. J. Bourhis, R. J. Gildea, J. A. K. Howard and H. Puschmann, *J. Appl. Crystallogr.*, 2009, **42**, 339–341.
40. G. M. Sheldrick, *SHELXT*, University of Göttingen and Bruker AXS GmbH, Karlsruhe, Germany, 2012–2018.
41. G. M. Sheldrick, *Acta Crystallogr.*, 2015, **A71**, 3–8.
42. G. M. Sheldrick, *SHELXL-20xx*, University of Göttingen and Bruker AXS GmbH, Karlsruhe, Germany, 2012–2018.
43. G. M. Sheldrick, *Acta Crystallogr.*, 2008, **A64**, 112-122.
44. G. M. Sheldrick, *Acta Crystallogr.*, 2015, **C71**, 3-8.
45. J. S. Rollett, in *Crystallographic Computing*, eds. F. R. Ahmed, S. R. Hall and C. P. Huber, Munksgaard, Copenhagen, Denmark, 1970, p. 167.
46. D. Watkin, in *Crystallographic Computing 4*, eds. N. W. Isaacs and M. R. Taylor, IUCr and Oxford University Press, Oxford, UK, Ch. 8 edn., 1988.
47. P. Müller, R. Herbst-Irmer, A. L. Spek, T. R. Schneider and M. R. Sawaya, in *Crystal Structure Refinement*, ed. P. Müller, Oxford University Press, Oxford, UK, Ch. 5 edn., 2006.
48. D. Watkin, *J. Appl. Crystallogr.*, 2008, **41**, 491-522.
49. A. Thorn, B. Dittrich and G. M. Sheldrick, *Acta Crystallogr.*, 2012, **A68**, 448-451.

50. A. Rodger, *Sci. Prog.*, 2008, **91**, 377-396.